Department of Physics and Astronomy
Heidelberg University

Bachelor Thesis in Physics
submitted by

Anniken Frønsdal Engedal

born in Oslo (Norway)

2024

The Enhanced Template Fit Method for Run-3 at ATLAS

This Bachelor Thesis has been carried out by Anniken Frønsdal Engedal at the
Kirchhoff-Institute for Physics in Heidelberg
under the supervision of
Prof. Dr. Hans-Christian Schultz-Coulon

Abstract

The Template Fit Method, implemented in ATLAS multi-boson analyses, applies templates to the different isolation energy (E_{iso}) distributions of promptly produced (real) and not promptly produced (fake) photons to estimate their relative contributions. Since E_{iso} is dependent on the transverse momentum (p_{T}) of the photons, and processes vary in p_{T} distributions, new templates are needed for each final state. A previous study generalised the templates for real and fake photons by investigating the correlation between E_{iso} and p_{T} of $Z\gamma$ and $Z\gamma\gamma$ final states under Run-2 conditions. However, whether such generalisation of templates can be extended to Run-3 and other final states remains an open question. This thesis aims to derive new general templates from $Z\gamma$ and $W\gamma$ final states under Run-3 conditions and applies these across different processes, such as $Z\gamma\gamma$ and $W\gamma\gamma$ final states to examine their potential universal applicability. The extracted templates exhibit good agreement with the E_{iso} distributions in various final states and with each other. Overall, the results strongly indicate that a generalised Template Fit Method can be successfully implemented in Run-3 environments and extended to electroweak final states with W bosons.

Kurzfassung

Die Template Fit Methode, die in ATLAS-Multibosonenanalysen implementiert wird, verwendet Templates für die unterschiedlichen Isolationsenergieverteilungen (E_{iso}) von prompt erzeugten (real) und nicht prompt erzeugten (fake) Photonen, um deren relativen Beiträge abzuschätzen. Da E_{iso} vom Transversalimpuls (p_{T}) der Photonen abhängt und verschiedene Prozesse unterschiedliche p_{T}-Verteilungen aufweisen, werden für jeden Prozess neue Templates benötigt. In einer vorherigen Studie wurde eine Verallgemeinerung der Templates für reale und fake Photonen entwickelt, indem die Korrelation zwischen E_{iso} und p_{T} der $Z\gamma$ und $Z\gamma\gamma$ Prozesse unter Run-2-Bedingungen untersucht wurde, wobei jedoch ungeklärt bleibt, ob diese Verallgemeinerung auf Run-3 und andere Prozesse erweitert werden kann. Diese Studie extrahiert allgemeine Templates aus $Z\gamma$ und $W\gamma$ Prozessen unter Run-3-Bedingungen und wendet sie auf verschiedene Prozesse an, wie die $Z\gamma\gamma$ und $W\gamma\gamma$ Prozesse, um ihre universelle Anwendbarkeit zu prüfen. Die Templates zeigen eine gute Übereinstimmung mit den E_{iso}-verteilungen in verschiedenen Prozessen und untereinander. Insgesamt deuten die Ergebnisse stark darauf hin, dass eine verallgemeinerte Template Fit Methode erfolgreich in Run-3 implementiert und auf elektroschwache Prozesse mit W Bosonen erweitert werden kann.

Contents

1 Introduction

The Standard Model (SM) of particle physics represents the attempt to explain the elementary constituents of matter. It is one of the best-tested theories in physics.

In the SM, the elementary constituents of matter are grouped into two different kinds of particles: fermions and bosons. Fermions are elementary matter particles called leptons and quarks. They occur in three generations with increasing mass. Interactions between fermions are mediated through bosons, which characterise the fundamental forces. In total, there are four fundamental forces. The electromagnetic force is carried by photons and describes the interactions of particles with electric charges. Furthermore, the strong force is responsible for the binding of quarks and is mediated by bosons called gluons. Interactions through the weak force are possible for short ranges and are mediated by the massive Z and $W^{\pm}$ bosons. At large scales, gravity is the dominating force, which is not included in the current SM [1].

The SM is tested in modern particle physics experiments that typically utilize the interaction of particles with matter for detection and identification purposes. One possibility is producing particles in high energy collisions, like at the Large Hadron Collider (LHC), located at CERN near Geneva. The accelerated protons or lead ions are focused in beams and arranged to collide at certain locations. At each collision point different detectors, such as the ATLAS detector, measure and analyse the resulting collision products. By studying the detector signatures the produced particles can be identified and their properties can be further examined [2].

One key aim of the ATLAS experiment is to investigate the electro-weak sector of the SM. This is done by analysing various weak interactions that produce Z, $W^{\pm}$ bosons, and photons in final states such as the $Z\gamma$, $W\gamma$, $Z\gamma\gamma$, and $W\gamma\gamma$ final states. A challenge in analysing data of such final states is estimating the background contribution of fake photons. Fake photons are photons that are not produced in the hard scattering interaction, mainly arising within the fragmentation of jets ($\pi^0 \to \gamma\gamma$), or are other particles misidentified as photons.

In order to distinguish between promptly produced (real) photons and fake photons the difference in the isolation energies of the two photons can be exploited. The isolation energy

of a photon describes the additional energy deposits around the photon. Fake photons have distributions of isolation energies, that shift to higher energies and are broader, compared to those of real photons. This is due to additional energy in the surroundings of fake photons arising from jet remnants. This distinction has been used in previous ATLAS analyses in the Template Fit Method to estimate the background contribution of fake photons. This method includes extracting templates for the isolation energy distributions of real and fake photons. The templates for real and fake photons are summed and fitted to data to obtain a proper normalisation. With this method, it is possible to estimate the individual contributions of real and fake photons for the final state under study.

Until recent studies, new templates had to be extracted for each studied final state to apply the Template Fit Method. This was due to the dependence of the isolation energy on the distribution of the transverse momentum (p_{T}) of the photon. The p_{T} distribution can vary across different final states, such as $Z\gamma$ and $W\gamma$, or in final states with multiple photons, like $Z\gamma\gamma$, where leading and subleading photons exhibit different p_{T} distributions. A recent study [3] on the final states $Z\gamma$ and $Z\gamma\gamma$ under Run-2 conditions attempted to solve this challenge by developing a generalisation of the isolation energy templates. In the study, the p_{T} dependence of the templates was examined. The template was factorised into a generic part and the final state-dependent p_{T} distribution of the photon. With this Enhanced Template Fit Method, it was possible to extract one template from the $Z\gamma$ final state that described the isolation energy distribution for both the $Z\gamma$ and $Z\gamma\gamma$ final state under Run-2 conditions.

In this thesis, the applicability of the Enhanced Template Fit Method to the $Z\gamma$ and $Z\gamma\gamma$ final states under Run-3 conditions is studied, and its potential extension to other final states including the W boson, such as the $W\gamma$ and $W\gamma\gamma$ processes. In Chapter 2, key elements of the ATLAS detector are discussed. Chapter 3 explains the photon reconstruction and identification procedures at ATLAS. After discussing the Template Fit Method and its enhancement in Chapter 4, new templates are generated for real and fake photons using the $Z\gamma$ and $W\gamma$ final states selected from Run-3 MC simulations in Chapter 5 and 6. Finally, the templates for real and fake photons are compared across different final states.

Author's Contribution

The analysis in this thesis involved a process with many different steps. It required many preparatory activities including data conversions and assessments of MC simulations. In this paragraph the author's contribution during this process is outlined.

The general procedure of the Enhanced Template Fit Method was already provided from a previous study on Run-2 data. For the preparation of the analysis in this thesis, I first affirmed key statements from the study on Run-2 data by reproducing many of its results using the same Monte Carlo (MC) simulations generated by Sherpa 2.2.10 as in the original study. For the analysis of the final states with real photons under Run-3 conditions, MC simulation samples were already provided. However, for the MC simulations needed for the analysis of the templates for fake photons, some samples proved to be incomplete. With the help of colleagues in my research group, new suitable samples were found and the data was collected. All the MC simulations used in this thesis were generated by Sherpa 2.2.14. The samples were provided in a PHYSLITE data format, which I converted using a provided code into accessible data formats (NTuples) for the software that I used. I checked the completeness and integrity of the samples, including, and in particular detail, after the data format conversions. This thesis utilised many different MC simulations, for which I performed the event selections. I conducted in total 10 different event selections of various signal and background MC simulations, many of which had not been studied by any means within the group yet. Therefore, I needed to investigate the samples and adjust certain criteria for the selections with the MC simulation samples used. After collecting the necessary MC simulations and assessing them, I implemented a new fit for final states under Run-3 conditions.

2 The Large Hadron Collider and the ATLAS Detector at CERN

The LHC [2] is built as a large ring, with a circumference of 27 km, around 100 m below the ground. Within the acceleration process, proton beams are preaccelerated, increasing the beam energy at each stage, until they are ultimately injected into the LHC. The LHC contains two separate proton beams that are bent onto a circular path by cooled superconducting magnets. They circulate in opposite directions and are stored for several hours in the ring. The two beams are crossed at four points, where particle detectors are located to detect the resulting collision products. To increase the luminosity, the protons are grouped in bunches that are focused on a width of a few μm. Each beam contains around 2800 bunches, with each bunch holding up to 10^{11} protons [4].

In 2022, a new period of data taking (Run-3) at CERN was initiated after several years of upgrading and maintenance work. Run-3 will last for four years at a newly achieved centre-of-mass energy of $\sqrt{s} = 13.6$ TeV. Run-3 is expected to deliver an integrated luminosity of $L_{\text{int}} = 250\ \text{fb}^{-1}$ [5], nearly double the amount of that achieved during Run-2 [6]. During the preparations for Run-3, the four detectors at LHC received major upgrades to their detector systems, computing infrastructure and to their data readout. The studies presented in this thesis utilise MC simulations under Run-3 conditions.

The ATLAS Experiment

The ATLAS detector [5, 7] is the largest detector at CERN. The full detector system in its current state is shown in Figure 1. The geometry of the detector [1] is outlined with spherical coordinates describing the plane transverse to the beam (z direction). The pseudorapidity η is typically used in place of the polar angle θ, defined by the equation:

$$\eta = -\log\left[\tan\left(\frac{\theta}{2}\right)\right]. \tag{1}$$

Angular distances can be expressed as:

$$\Delta R = \sqrt{(\Delta\eta)^2 + (\Delta\phi)^2}. \tag{2}$$

With these coordinates, relevant variables like the transverse energy of a particle E_{T} can be defined as:

$$E_{\mathrm{T}} = \frac{E}{\cosh \eta} \tag{3}$$

with E describing the particle's energy.

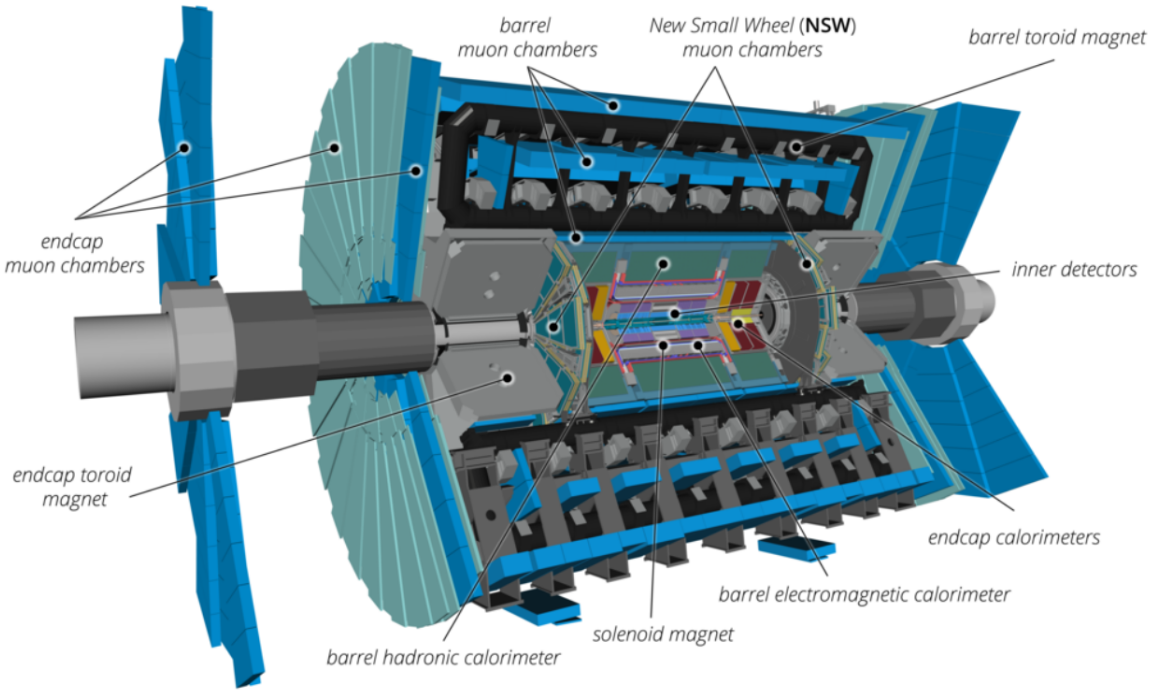

Figure 1: Cut-away schematic overview of the whole ATLAS detector after Run-3 installations. Taken from [8].

ATLAS is a general-purpose detector, recording data for many different research sectors in particle physics. With energies reaching to TeV scale and high integrated luminosity, it is possible to explore rare electro-weak final states. The detector is built concentrically in different layers around the collision point that makes it possible to identify the particles and record their trajectory, momentum and energy.

The Inner Detector

The Inner Detector [9] is build around the proton beam at the collision point. It is placed in a 2 Tesla solenoidal magnetic field, which is parallel to the beam. The Inner Detector measures the momentum of charged particles and allows vertex and track reconstruction. In the innermost part, compact layers of silicon pixels measure the trajectory by detecting signals of energy deposits created by the charged particles. In the middle of the detector lies the Semiconductor Tracker consisting of over 4000 modules of 6 million micro-strips of silicon sensors. They allow the reconstruction of tracks of charged particles with a very high resolution. The outermost part of the Inner Detector features around 300000 thin-walled drift tubes filled with a gas mixture. With ionisation and transition radiation effects, it is possible to both reconstruct tracks of particles and identify them.

The Calorimeters

A Calorimeter performs measurements of the energy of particles. Incoming particles are absorbed by a passive medium, producing showers that ionise an active medium. The ionisation can be converted into an electric current, generating a signal, from which the energy of the particles can be derived.

- **The electromagnetic (EM) calorimeter** [7] at ATLAS uses lead as the passive medium and liquid Argon (LAr) as the active medium. The LAr is sandwiched between layers of lead. In η direction, the EM calorimeter is composed of a barrel section ($|\eta| < 1.475$), two end caps ($1.375 < |\eta| < 3.2$) and LAr forward calorimeter ($3.1 < |\eta| < 4.9$). The EM calorimeter features layers with varying thicknesses across different $|\eta|$ regions, providing very fine granularity. This fine granularity enables highly precise energy measurements and spatial resolution.

- **The hadronic calorimeter** [10] at ATLAS measures the energy of hadrons that do not deposit all their energy in the EM calorimeter. Incoming hadrons interact with steel tiles, creating showers of new particles. The shower is detected with plastic scintillator tiles, that produces photons. These photons induce an electric signal, with the intensity being proportional to the energy of the shower. Just like for the EM calorimeter, the hadronic calorimeter is extended by a LAr hadronic endcap at $1.5 < |\eta| < 3$ and LAr forward calorimeters up to $|\eta| < 4.9$.

The Inner Detector and calorimeters together build a detector system which collects enough data to accurately identify incoming particles such as electron and photons. An electron passing through the different layers of the detector is illustrated in Figure 2.

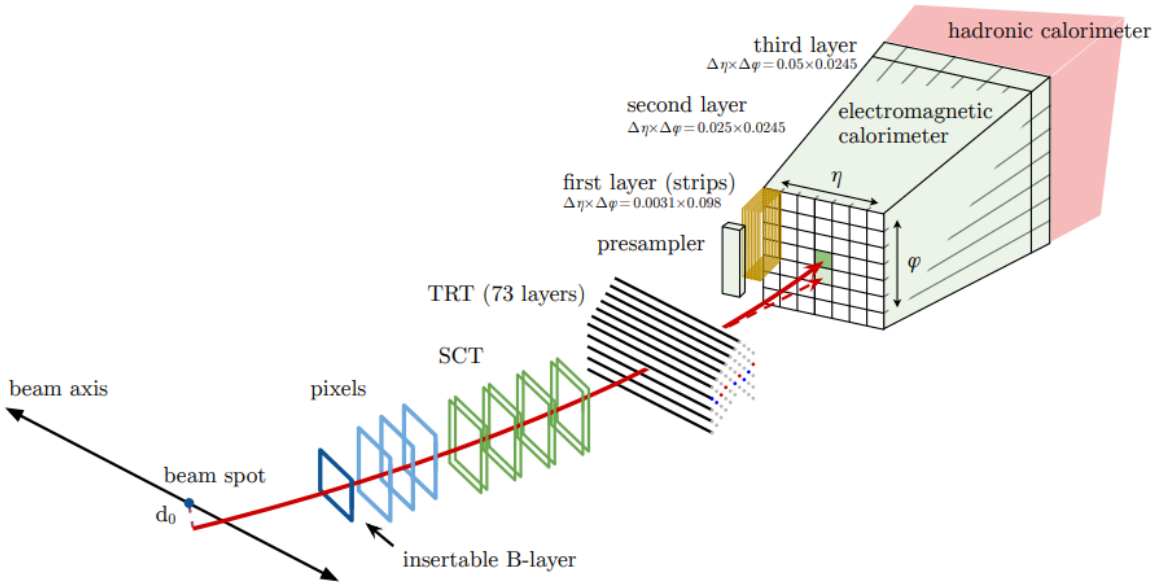

Figure 2: Schematic path of an electron in the detector. The dashed red line illustrates the path of a photon produced by interaction of the electron with detector materials. The electron first passes through the Inner Detector. It consists of silicon pixels, the Semiconducter Tracker (SCT) and the Transition Radiation Tracker (TRT) that perform measurements to identify and reconstruct the track of the electron. After the Inner Detector, the electron passes through the EM and hadronic calorimeter. Here, the electron is absorbed and produces showers from which its energy can be derived. Taken from [8].

The Muon Spectrometer

Muons are one of the few particles that cross the thick layers of the calorimeters. This is why the outer layer of ATLAS is built for the detection of muons. In the muon spectrometer [7], five different detector technologies serve the identification and measurement of the transverse momentum of the muon. Three large toroid magnets create the magnetic field needed inside the muon spectrometer. Precision detectors determine the position of the muons and Fast-Response Detectors the momenta.

3 Photon Reconstruction and Identification at ATLAS

Different particles leave distinct patterns when passing through the detector. From these signature trajectories, the particles can be reconstructed and identified. Since this thesis studies final states with photons, the focus of this chapter lies on the reconstruction of photons. Photons can be reconstructed and classified based on their energy deposits in the calorimeters and the track information from the Inner Detector.

3.1 Photon Reconstruction

The reconstruction of photons and electrons starts with the construction of topo-clusters using a set of threshold conditions, commonly named the "4-2-0" algorithm [11]. It firstly involves the summation of calorimeter cells above a certain significance threshold $|\zeta_{\text{cell}}| \geq 4$, where the significance is defined as:

$$\zeta_{\text{cell}} = \frac{E_{\text{cell}}}{\sigma_{\text{noise,cell}}}. \tag{4}$$

Here, E_{cell} stands for the energy and $\sigma_{\text{noise,cell}}$ for the noise of a cell in the calorimeter. Next, neighbouring cells are successively added to the cluster if they exceed a threshold of $|\zeta_{\text{cell}}| > 2$. If the condition is fulfilled, the cell serves as a seed cell, and the iteration continues for this cell. Once the condition is not fulfilled, the remaining neighbouring cells with $|\zeta_{\text{cell}}| \geq 0$ are added. All together, these cells form topological clusters or topo-clusters.

For the reconstruction, only topo-clusters above the threshold of $E_{\text{topo}}^{\text{EM}} > 400\,\text{MeV}$ and with $f_{\text{EM}} = \frac{E_{\text{topo}}^{\text{EM}}}{E_{\text{topo}}^{\text{total}}} > 0.5$ are considered. Here, $E_{\text{topo}}^{\text{EM}}$ is the energy of the topo-cluster only in the EM calorimeter and $E_{\text{topo}}^{\text{total}}$ is the total energy of the topo-cluster.

These reconstructed topo-clusters are then matched to possible tracks in the Inner Detector. Different particles produce distinct tracks in the Inner Detector, such as electrons that generate hits within the Inner Detector material. Photons can leave different signatures in the detector, depending on their interaction with the detector materials, called *unconverted* and *converted* photons. The expected tracks and cluster formations of converted and unconverted photons are displayed in Figure 3. Unconverted photons leave no track in the

Inner Detector. Thus the topo-clusters produced by the energy deposits in the calorimeter can not be matched to a track or vertex. Converted photons have interacted with the detector material before reaching the calorimeters, resulting in the production of an e^+e^--pair. Therefore the clusters can be matched to two tracks in the Inner Detector and a conversion vertex. In addition to the signatures shown in Figure 3, photons may also interact with the detector materials through Compton-scattering that would only leave a single track in the Inner Detector.

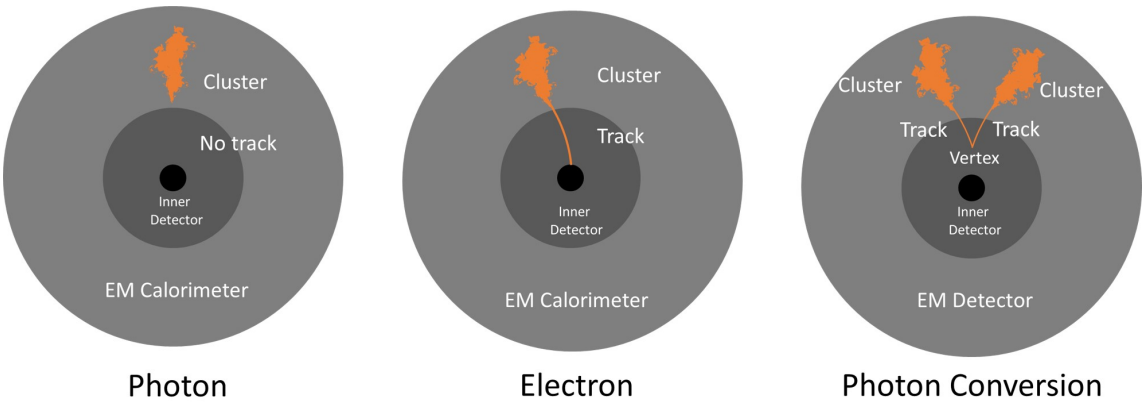

Figure 3: The signatures of photons, electrons and photon conversions in the Inner Detector and EM calorimeter of the ATLAS detector. Unconverted photons leave no track in the Inner Detector but produce a cluster in the calorimeters. Photons can interact with the detector materials and convert into a e^+e^--pair that leave two tracks in the Inner Detector. In the case of Compton-scattering, the calorimeter cluster can be matched to only one track in the Inner Detector. Taken from [12].

After track matching, the topo-clusters are then sorted with respect to their transverse energy. The topo-cluster with the highest energy is selected as the starting point of the construction of so-called super-clusters. A topo-cluster can be used as a seed for a super-cluster, if it has an energy above $E_{\mathrm{T}}^{\mathrm{EM}} > 1.5$ GeV. Topo-clusters in the region $\eta \times \phi = 0.075 \times 0.125$ around the super-cluster seed's barycentre are added to the super-cluster and are referred to as satellite clusters. A cluster can not be used as a seed cluster if it has already been added as a satellite cluster to another super-cluster. Finally, the energies are calibrated and corrections for the position are carried out. By matching the final super-clusters to tracks and conversion vertices in the Inner Detector, the particles can be identified.

3.2 Photon Identification

Photon identification (ID) [13] aims to distinguish between promptly produced photons (real photons) and fake photons and can be used to reject background objects. Promptly produced photons originate from the hard scattering process. Fake photons are all reconstructed photons that are not promptly produced or other objects reconstructed as photons such as electrons or narrow jets. The most dominate process that contributes to the fake background of reconstructed photons are photons arising within jet fragmentations. Most of these fake photons are produced in the decay of neutral pions $\pi^0 \to \gamma\gamma$.

A way to distinguish real from fake photons, is by exploiting the different shower shapes in the calorimeters. The variables describing the development of the showers are referred to as shower shape variables. The definitions of the shower shape variables are illustrated in Figure 35 in Appendix A. They outline the lateral and longitudinal EM calorimeter showers and their leakage fractions into the hadronic calorimeter. Compared to fake photons, real photons have narrower energy deposits in the EM calorimeter and less leakage into the hadronic calorimeter. This is due to the fact that fake photons most likely emerge from jet fragmentations and therefore have more particles in their nearby surroundings. If fake photons are produced in a neutral pion decay $\pi^0 \longrightarrow \gamma\gamma$, typically two nearby energy maxima can be found in the first layer of the EM calorimeter. ATLAS defines different ID criteria including Loose-, Medium- and Tight ID, based on certain selection cuts on the shower shape variables that are listed in Table 4 in Appendix A. The different ID criteria correspond to increasingly strict requirements, that can be used for different analyses [14].

3.3 Photon Isolation

Despite the complex procedure of photon reconstruction and additional identification, the information is still not sufficient to confidently discriminate fake photons from real photons. In this final step of the identification procedure, the concept of isolation energy proves useful. Fake photons have higher energy deposits in their surroundings compared to promptly produced photons. This is due to additional energies arising from jet remnants. To quantify this distinction, the isolation energy is constructed. In the EM calorimeter and Inner Detector, two different types of isolation quantities can be obtained [15].

- **Track Isolation**: A cone centred around the candidate photon is constructed with a given radius ΔR. All the additional tracks within the cone are summed up to create the variable track isolation $p_{\mathrm{T}}^{\mathrm{coneXX}}$ (XX stands for the cone radius ΔR multiplied by a factor 100). Since in this analysis only the calorimeter isolation is considered, track isolation will not be discussed in depth, but further details are provided in [15].

- **Calorimeter Isolation**: The construction of the isolation energy in the EM calorimeter follows a similar strategy to the construction of the track isolation and is illustrated in Figure 4. A cone with radius $\Delta R = 0.2$ is assembled around the barycentre of the photon cluster. Subsequently, the transverse energies ($E_{\mathrm{T}}^{\mathrm{EM}}$) of the topo-clusters with barycentres located inside the cone are summed up:

$$E_{\mathrm{T,raw}}^{\mathrm{cone20}} = \sum_{\mathrm{cone}} E_{\mathrm{T}}^{\mathrm{EM}}. \tag{5}$$

  Since only the additional energy in the cone should be considered, the energy coming from the photon itself ($E_{\mathrm{T,core}}$), needs to be subtracted from the sum of energies ($E_{\mathrm{T,raw}}^{\mathrm{cone20}}$). The energy of the photon candidate corresponds to a rectangular cluster with calorimeter cells 5×7 positioned at the barycentre of the photons cluster. In terms of η and ϕ, the rectangular cluster corresponds to a $0.125 \times 0,175$ window, represented by the yellow rectangle in Figure 4. Finally, the sum of energies has to be corrected for any excess energies arising from leakage and pile-up [15]:

$$E_{\mathrm{T}}^{\mathrm{cone20}} = E_{\mathrm{T,raw}}^{\mathrm{cone20}} - E_{\mathrm{T,core}} - E_{\mathrm{T,leakage}} - E_{\mathrm{T,pile-up}}. \tag{6}$$

To define requirements for the isolation of a photon, ATLAS recommends specific working points (WP) for both track and calorimeter isolation. For a variable cone size of $\Delta R = 0.2/0.4$, ATLAS establishes three WPs, shown in Table 1. For a photon to pass the Loose WP, the isolation energies have to satisfy following requirements:

$$p_{\mathrm{iso}} := p_{\mathrm{T}}^{\mathrm{cone20}} - 0.065 \cdot p_{\mathrm{T}} < 0, \tag{7}$$

$$E_{\mathrm{iso}} := E_{\mathrm{T}}^{\mathrm{cone20}} - 0.065 \cdot p_{\mathrm{T}} < 0. \tag{8}$$

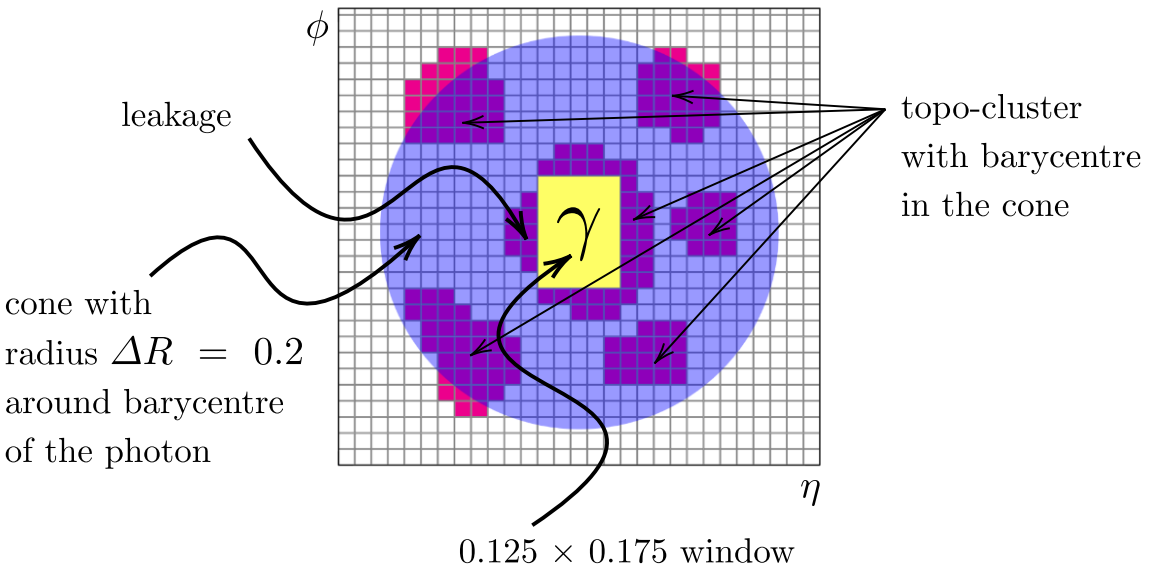

Figure 4: Schematic overview of the construction of $E_{\mathrm{T}}^{\mathrm{cone20}}$ (slice in the EM calorimeter in the $\eta \times \phi$ plane). The magenta coloured cells represent the topo-clusters in the EM calorimeter. The purple circle shows the range of the assembled cone ($\Delta R = 0.2$) with the candidate photon cluster in the centre. To determine the cone energy $E_{\mathrm{T}}^{\mathrm{cone20}}$, the energy of all the topo-clusters with barycentres within the cone are summed up. To only get the additional energy around the photon, the sum of topo-cluster energies is subtracted by the energy of the photon, which is represented by the yellow rectangle in the figure. The cone energy $E_{\mathrm{T}}^{\mathrm{cone20}}$ is corrected for leakage (magenta cells around yellow rectangle) and excess energy from pile-up. Taken from [3].

Table 1: Definition of the ATLAS recommended photon isolation WPs (Loose, Tight, TightCaloOnly). Taken from [11].

Working point	**Calorimeter isolation**	**Track isolation**
Loose	$E_{\mathrm{T}}^{\mathrm{cone20}} < 0.065 \times E_{\mathrm{T}}$	$\frac{p_{\mathrm{T}}^{\mathrm{cone20}}}{E_{\mathrm{T}}} < 0.05$
Tight	$E_{\mathrm{T}}^{\mathrm{cone40}} < 0.022 \times E_{\mathrm{T}} + 2.45$ GeV	$\frac{p_{\mathrm{T}}^{\mathrm{cone20}}}{E_{\mathrm{T}}} < 0.05$
TightCaloOnly	$E_{\mathrm{T}}^{\mathrm{cone40}} < 0.022 \times E_{\mathrm{T}} + 2.45$ GeV	—

4 Enhanced Template Fit Method

4.1 Template Fit Method

The Template Fit Method, as established in previous multi-boson analyses at ATLAS, is an approach to estimate the fake photon background in a given final state. The idea of the method is to exploit the different shapes of the E_{iso} distributions of real and fake photons. The differences can be seen in Figure 5, illustrating the general idea of the Template Fit Method. The E_{iso} distribution for fake photons is shifted to larger energies and is broader with respect to that of real photons. The shapes of the distributions are fixed for real and fake photons with templates derived separately from the corresponding MC simulations. The sum of the templates is fitted to data, to determine the normalisation of the distributions. By integrating the templates from $-\infty$ to 0 according to the Loose WP as defined in Table 1, it is possible to estimate the individual contributions of real and fake photons in the studied final state.

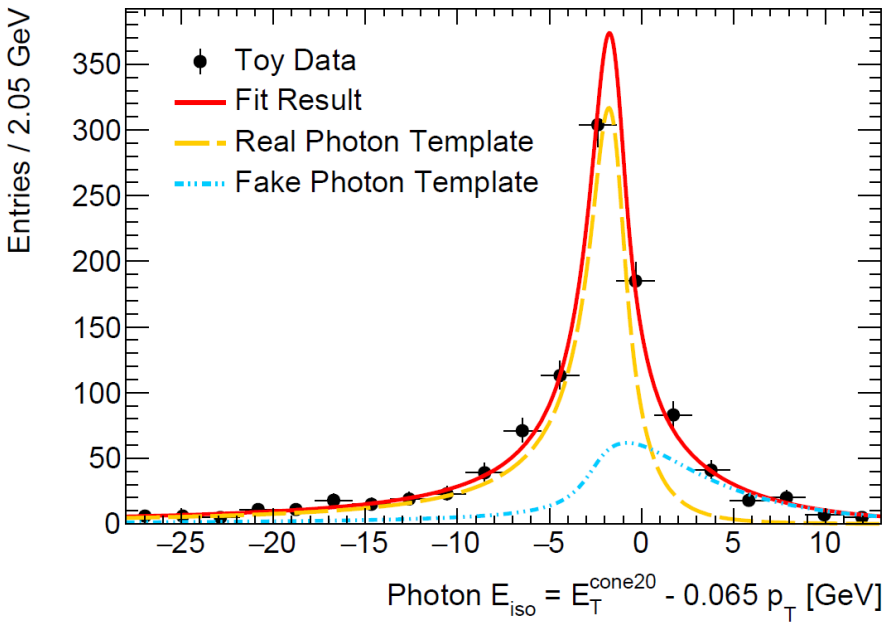

Figure 5: Illustration of the Template Fit Method with toy data. The shapes of the E_{iso} distributions of real and fake photons are derived from MC simulations and subsequently fixed with corresponding templates. The sum of the templates (red line) is fitted to data to determine the normalisation factors. The individual contributions of real and fake photons can be estimated via integration from $-\infty$ to 0 of E_{iso} according to the Loose WP. Taken from [3].

4.2 Generalisation of the Template Fit Method

In previous analyses, such as [16], an individual template extraction was required for each final state to implement the Template Fit Method. This was due to a strong p_{T} dependence of the E_{iso} distribution for both real and fake photons. The p_{T} dependence of the E_{iso} distribution for real photons for the $Z\gamma$ final state is demonstrated exemplary in Figure 6. The figure shows the E_{iso} distribution for different p_{T} intervals of the photon. The peak of the distribution drifts to lower energies with increasing p_{T}, largely due to the subtraction of $0.065 \cdot p_{\mathrm{T}}$ in the definition of E_{iso}, as can be seen in Equation 8. In addition, the width of the distribution broadens with higher p_{T} values.

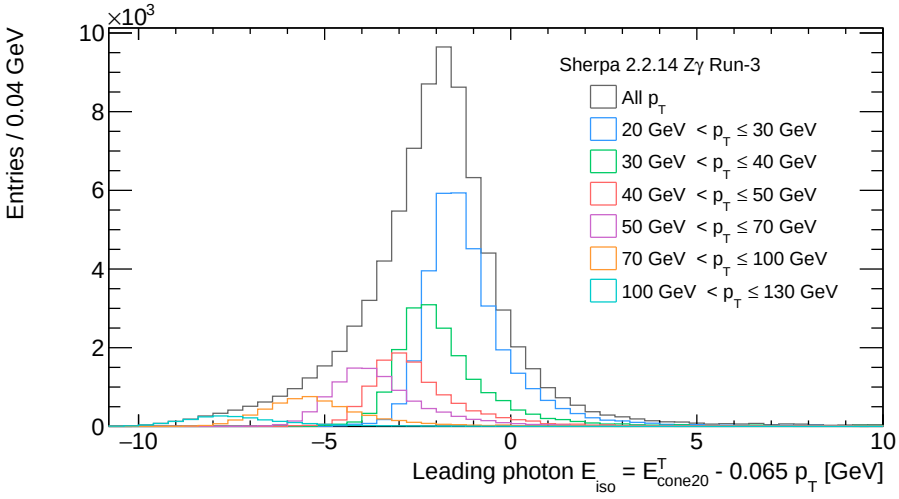

Figure 6: The E_{iso} distribution of the leading photon in the $Z\gamma$ final state under Run-3 conditions for different p_{T} intervals. The E_{iso} distributions shift to lower energies with increasing p_{T}, mainly due to the subtraction of $0.065 \cdot p_{\mathrm{T}}$ in the definition of E_{iso} as shown in Equation 8, and broaden.

Further, the p_{T} dependence of the E_{iso} distribution for fake photons is displayed exemplary for the $W\gamma$ final state in Figure 7. Comparable to the E_{iso} distributions observed for real photons, the E_{iso} distribution for fake photons also broadens with increasing p_{T} and shows a slight shift towards lower energies. However, this shift is less pronounced than that observed for real photons in Figure 6.

Since different processes exhibit different p_{T} distributions, the E_{iso} distributions also have different shapes, as demonstrated in Figure 8 for final states under Run-3 conditions. Consequently, the different final states require individual isolation templates. This is also the case for leading and subleading photons in final states with multiple photons as displayed in Figure 9.

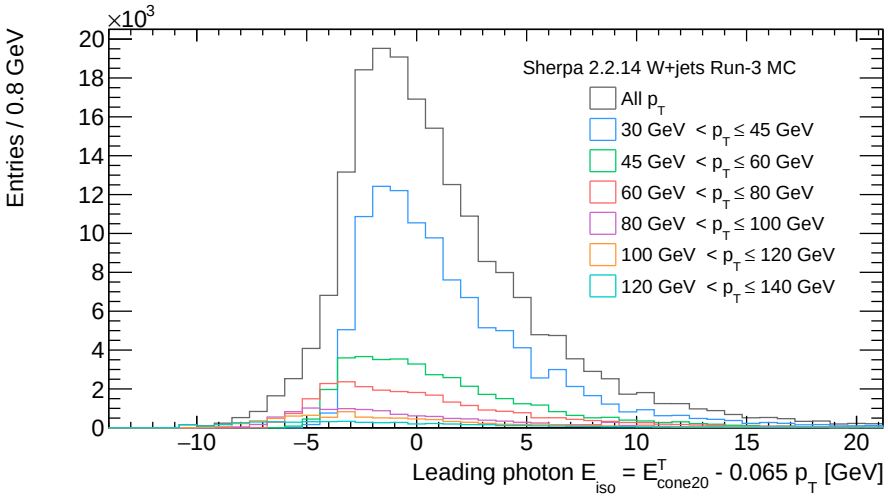

Figure 7: E_{iso} distribution for the $W\gamma$ final state under Run-3 conditions, with a fake final state photon for different p_{T} intervals. The E_{iso} distribution of fake photons exhibits a dependence on p_{T} . The distribution broadens for larger p_{T} values and shows a slight shift to lower energies.

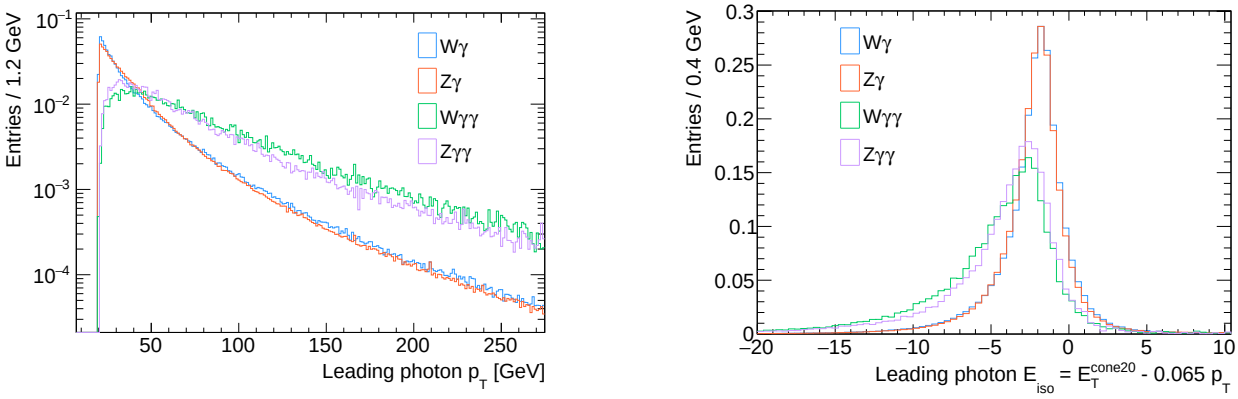

Figure 8: The p_{T} and E_{iso} distribution of the leading photon is shown for different final states under Run-3 conditions.

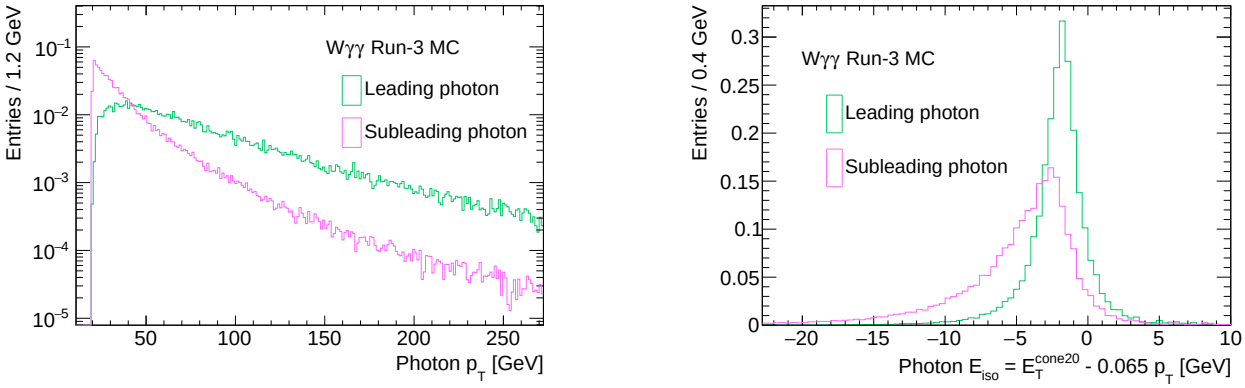

Figure 9: The p_{T} and E_{iso} distributions of leading and subleading photon is depicted for the $W\gamma\gamma$ final state under Run-3 conditions.

The p_{T} dependence of the E_{iso} distribution of real and fake photons was investigated in a previous study on Run-2 data. In the study, a generalised template extraction method was introduced, as described in the following paragraphs [3]. The generalisation of the Template Fit Method involves the factorisation of the E_{iso} template into a generic and a final state-dependent part to separate the p_{T} dependence of the E_{iso} distribution:

$$T_{\gamma,j}(E_{\mathrm{iso}}, p_{\mathrm{T}} \mid \vec{\theta}) \times f_X(p_{\mathrm{T}}). \tag{9}$$

Here, γ stands for real photons and j for fake photons. $T_{\gamma,j}$ is the generic part of the template and represents a two-dimensional model describing the correlation between E_{iso} and p_{T} with the parameters $\vec{\theta}$. Ideally, $T_{\gamma,j}$ should be consistent across different final states for real and fake photons. To account for the different p_{T} distributions of the final state photons, the generic template is multiplied by the final state-dependent p_{T} distribution $f_X(p_{\mathrm{T}})$ of the studied final state X.

The E_{iso} templates can be derived by performing a two-dimensional maximum likelihood fit of the (E_{iso}, p_{T}) distribution to the two-dimensional model $T_{\gamma,j}$. The likelihood function $\mathcal{L}$ takes the following form:

$$\mathcal{L}(\vec{\theta} \mid E_{\mathrm{iso}}, p_{\mathrm{T}}) = \prod_{i=1}^{n} T_{\gamma,j}(E_{\mathrm{iso},i}, p_{\mathrm{T},i} \mid \vec{\theta}) \cdot f_X(p_{\mathrm{T},i}), \tag{10}$$

with $(E_{\mathrm{iso},i}, p_{\mathrm{T},i})$ representing the values for E_{iso} and p_{T} for the i-th event of the MC simulations for the final state X. The product in the likelihood function is taken over all events $i \in (1, ..., n)$. The optimal parameters $\vec{\theta}_{\mathrm{opt}}$ can be determined by maximising the likelihood function:

$$\vec{\theta}_{\mathrm{opt}} = \arg\max_{\vec{\theta}} \mathcal{L}(\vec{\theta} \mid E_{\mathrm{iso}}, p_{\mathrm{T}}). \tag{11}$$

The E_{iso} template $\mathcal{T}_{\gamma,j}(E_{\mathrm{iso}})$ can then be obtained by projecting the two-dimensional fit onto the E_{iso} axis:

$$\mathcal{T}_{\gamma,j}(E_{\mathrm{iso}})_X := \int_0^{\infty} T_{\gamma,j}(E_{\mathrm{iso}}, p_{\mathrm{T}} \mid \vec{\theta}_{\mathrm{opt}}) \cdot f_X(p_{\mathrm{T}})\, \mathrm{d}p_{\mathrm{T}}. \tag{12}$$

It is expected, that the same optimal parameters $\vec{\theta}_{\mathrm{opt}}$ derived with the final state X, provides a good description for the template of another final state Y. The only necessary

modification is to replace the p_{T} distribution of X to that of the final state Y:

$$\mathcal{T}_{\gamma,j}(E_{\mathrm{iso}})_Y := \int_0^\infty T_{\gamma,j}(E_{\mathrm{iso}}, p_{\mathrm{T}} \mid \vec{\theta}_{\mathrm{opt}}) \cdot f_Y(p_{\mathrm{T}})\,\mathrm{d}p_{\mathrm{T}}. \tag{13}$$

In [3] the optimal parameters $\vec{\theta}_{\mathrm{opt}}$ for the generic model $T_{\gamma,j}$ were extracted from the $Z\gamma\gamma$ final state from Run-2 MC simulations. By multiplying the generic template by the corresponding p_{T} distribution of the studied final state, the isolation template could be obtained through projection onto the E_{iso} axis. The obtained template described the E_{iso} distribution for the $Z\gamma$ and $Z\gamma\gamma$ final states under Run-2 conditions. The extracted template sufficed to estimate the fake contributions to the background for the $Z\gamma$ and $Z\gamma\gamma$ final states. The following analysis studies the application of this Enhanced Template Fit Method to various final states under Run-3 conditions.

5 Templates for Real Photon Candidates

Even though the photon ID and isolation requirements for reconstructed photons remain unchanged in Run-3 with respect to Run-2 [17], it is nevertheless necessary to extract new optimal parameters $\vec{\theta}_{\text{opt}}$ for the generic part of the template when studying final states under Run-3 conditions. This is due to the pile-up dependence of the E_{iso} distributions, as demonstrated in Figure 10 for the $Z\gamma$ final state. In the figure the E_{iso} distribution is shown for different intervals of the number of simultaneous interactions per bunch crossing μ. It is observed that the E_{iso} distribution gets broader with higher μ values. Since the distribution of μ differs between Run-2 and Run-3 as can be seen in Figure 11, it is necessary to derive new templates.

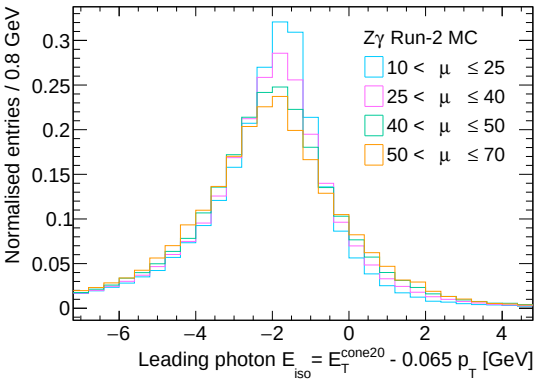

Figure 10: The E_{iso} distribution of the leading photon in the $Z\gamma$ final state under Run-2 conditions for different intervals of μ. The E_{iso} distribution shows a dependence on μ. The distribution broadens with higher μ values.

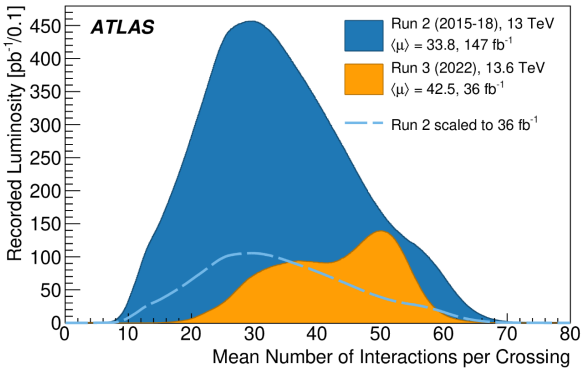

Figure 11: The integrated luminosity as a function of μ for Run-2 (blue) and Run-3 (orange) collision data. Run-2 and Run-3 show different μ distributions. The blue dashed line represents the distribution for Run-2, normalised to the integral of the Run-3 distribution. Taken from [18].

This chapter studies the application of the Enhanced Template Fit Method, as explained in Section 4.2, to real photons in different final states under Run-3 conditions, namely the $Z\gamma$, $W\gamma$, $Z\gamma\gamma$ and $W\gamma\gamma$ final states. The templates are extracted from the $Z\gamma$ and $W\gamma$ final states, because they offer significantly higher statistics than the $Z\gamma\gamma$ and $W\gamma\gamma$ final states and thereby allow for better fit stability. Finally, the extracted templates are compared to the other final states.

5.1 Event Selections

All MC simulations that are used in this thesis are listed in Table 5 in Appendix B.

$Z\gamma$ and $Z\gamma\gamma$ Selection

The $Z\gamma$ and $Z\gamma\gamma$ final states in this analysis represent the leptonic decay of a Z boson with one and two final state photons. The photons can be radiated at leading order either from one of the leptons (final state radiation: FSR) or from the initial quark line (initial state radiation: ISR). The corresponding Feynman diagrams for ISR final states are depicted in Figures 12 and 13. The $Z\gamma$ and $Z\gamma\gamma$ events are selected according to the criteria listed in

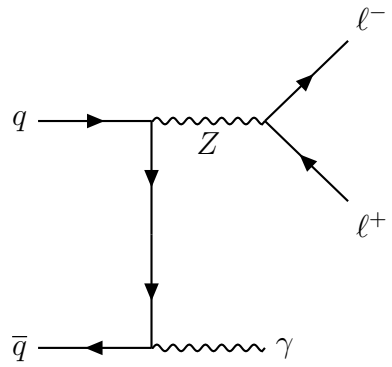

Figure 12: Feynman diagram of the $Z\gamma$ final state. A Z boson decays into a lepton pair ($\ell^+\ell^-$) with one final state photon produced as ISR.

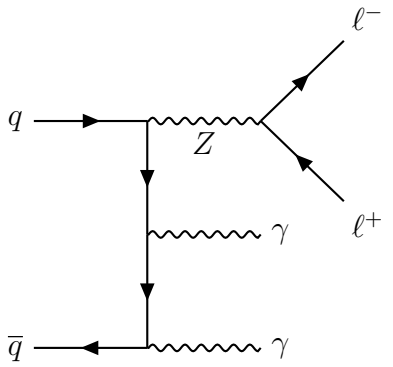

Figure 13: Feynman diagram of the $Z\gamma\gamma$ final state. A Z boson decays into a lepton pair ($\ell^+\ell^-$) with two final state photons produced as ISR.

Table 2. Electrons, muons, and photons need to satisfy certain p_{T}, η, and identification (ID) or isolation (ISO) requirements. To select only ISR final states, an FSR rejection is performed as illustrated in Figure 14. The FSR rejection requires an event to satisfy the following criteria:

$$m_{l_1 l_2} + \min(m_{l_1 l_2 \gamma_1}, m_{l_1 l_2 \gamma_2}) > 2 \cdot m_Z. \tag{14}$$

Here, l_1 (γ_1) denotes the leading lepton (photon) in p_{T} and l_2 (γ_2) the subleading lepton (photon). $m_{l_1 l_2}$ stands for the invariant mass of the lepton pair and $m_{l_1 l_2 \gamma_1}$ ($m_{l_1 l_2 \gamma_2}$) stands for the three-body invariant mass of the leptons together with the leading (subleading) photon. The mass of the Z boson is represented by m_Z. If the event has a photon produced as FSR, the invariant mass $m_{l_1 l_2} < m_Z$ and the invariant masses $m_{l_1 l_2 \gamma_1}, m_{l_1 l_2 \gamma_2} \leq m_Z$. Therefore the inequality in Equation 14 is not fulfilled and the event is rejected.

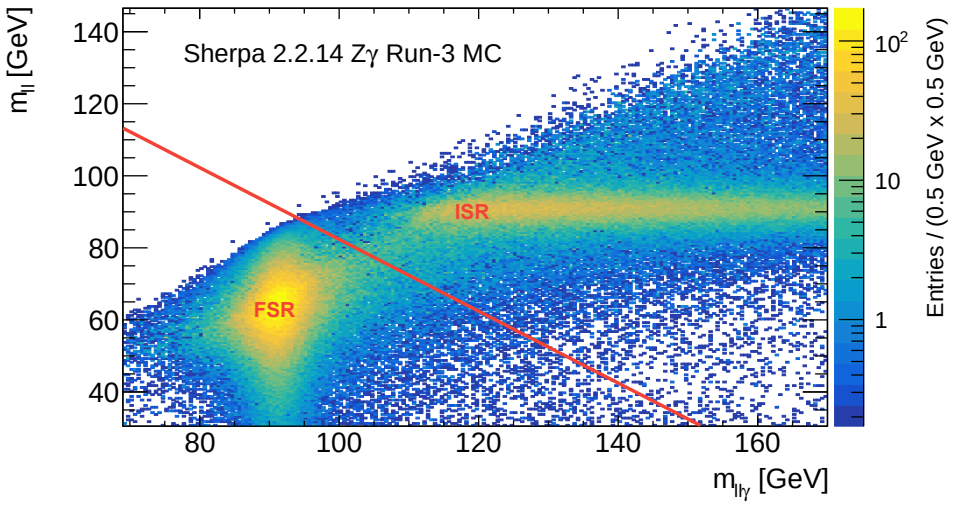

Figure 14: Illustration of the FSR rejection in the selection of the $Z\gamma$ and $Z\gamma\gamma$ final states. The correlation between the three-body invariant mass of the leptons and the final state photon $m_{ll\gamma}$ and the two-body invariant mass of the lepton-pair m_{ll} is displayed for $Z\gamma$ MC simulations under Run-3 conditions. The majority of FSR events are observed around $m_{ll\gamma} = m_Z$ with $m_{ll} < m_Z$. ISR events are clustered around $m_{ll} = m_Z$ with $m_{ll\gamma} \geq m_Z$. The red line illustrates the FSR rejection, vetoing all events below the line.

Table 2: Summary of the criteria applied for the event selection of the $Z\gamma$ and $Z\gamma\gamma$ final states. For the $Z\gamma$ final state, only the selection is performed for γ_1. The selection is finalised with a truth match based on the truth information of the sample.

Leptons	**Electrons**
	$p_T(l_1) \geq 30$ GeV, $p_T(l_2) \geq 20$ GeV
	$\lvert\eta\rvert < 1.37$, or $1.52 < \lvert\eta\rvert < 2.47$
	Tight ID (l_1)
	Muons
	$p_T(l_1) \geq 30$ GeV, $p_T(l_2) \geq 20$ GeV
	$\lvert\eta\rvert < 2.5$
	Tight ISO (l_1)
	Both
	at least 2 leptons ($e^{\pm}, \mu^{\pm}$) same flavour, opposite charge
	invariant mass $m_{l_1 l_2} > 40$ GeV
Photons	$Z\gamma$: at least 1 photon, $Z\gamma\gamma$: at least 2 photons
	$p_T(\gamma_1)$, $p_T(\gamma_2) \geq 20$ GeV
	$\lvert\eta\rvert < 1.37$ or $1.52 < \lvert\eta\rvert < 2.37$
	Tight ID
	$\Delta R(\gamma_1, \gamma_2) > 0.4$
Combined	ISR: $m_{l_1 l_2} + \min(m_{l_1 l_2 \gamma_1}, m_{l_1 l_2 \gamma_2}) > 2 \cdot m_Z$

$W\gamma$ and $W\gamma\gamma$ Selection

The quark-antiquark annihilation may also produce $W^{\pm}$ bosons that promptly decay into a lepton and neutrino. In the $W\gamma$ and $W\gamma\gamma$ final states, one and two photons are radiated either as ISR or FSR. The ISR final states are illustrated in the Feynman diagrams in Figure 15 and 16. The criteria applied to the selection of the $W\gamma$ and $W\gamma\gamma$ final states

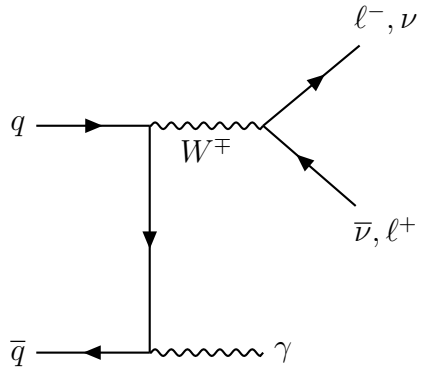

Figure 15: Feynman diagram of the $W\gamma$ final state. A W boson decays into a lepton-neutrino pair with one photon produced as ISR.

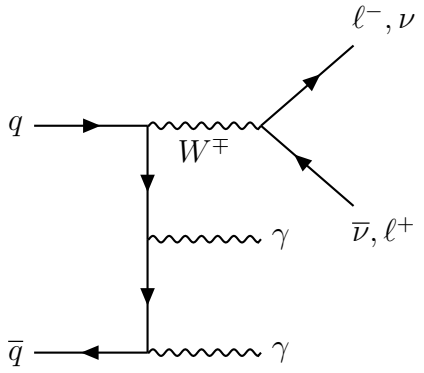

Figure 16: Feynman diagram of the $W\gamma$ final state. A W boson decays into a lepton-neutrino pair with two photons produced as ISR.

are summarised in Table 3. Similar to the event selection of the $Z\gamma$ and $Z\gamma\gamma$ final states, p_{T}, η, ID and ISO requirements are placed on the electrons, muons, and photons. To exclude events with Z bosons, a $Z(\gamma)$ veto is triggered by forcing the invariant mass of the lepton and photon(s) $m_{l\gamma(\gamma)}$ to be outside a certain region around the Z boson mass. Since the $W\gamma$ and $W\gamma\gamma$ final states only decay into one lepton and additionally the neutrino energy is unavailable, it is more challenging to distinguish signal events from background events. For this reason, an additional selection criterion is applied to the transverse impact parameter d_0, its uncertainty σ_{d_0} and the longitudinal impact parameter z_0 to reduce the background events. The definitions of z_0, d_0, and σ_{d_0} and further details can be found in [7]. Since the energy of the neutrino is unavailable, requirements are instead applied to the missing transverse energy $E_{\mathrm{T}}^{\mathrm{miss}}$ which corresponds to the expected energy of the neutrino. Furthermore, the event selections of the $W\gamma$ and $W\gamma\gamma$ final states do not include an FSR rejection, like for the selections of the $Z\gamma$ and $Z\gamma\gamma$ final states. The reason for this is the unavailability of the two-body invariant mass of the lepton-neutrino pair, $m_{l,\nu}$. Instead a selection criterion is applied to the transverse mass of the W boson, m_{T}^{W}.

Table 3: Summary of the selection criteria in the event selections of the $W\gamma$ and $W\gamma\gamma$ final states. For the $W\gamma\gamma$ final state all the requirements are applied to both final state photons. Further information about the LHMedium ID selection criterion for electrons can be found in [19]. The selection is finalised with a truth match based on the truth information of the MC simulation.

Leptons	**Electrons**
	$p_{\mathrm{T}} > 25$ GeV, $\lvert\eta\rvert < 2.47$, exclude $1.37 < \lvert\eta\rvert < 1.52$
	LHMedium ID, Tight ISO
	$\lvert z_0 \sin\theta\rvert < 0.5$ mm, $\lvert\frac{d_0}{\sigma_{d_0}}\rvert < 5$
	Muons
	$p_{\mathrm{T}} > 25$ GeV, $\lvert\eta\rvert < 2.5$
	Medium ID, Tight ISO
	$\lvert z_0 \sin\theta\rvert < 0.5$ mm, $\lvert\frac{d_0}{\sigma_{d_0}}\rvert < 3$
	Both
	at least 1 lepton ($e^{\pm}, \mu^{\pm}$)
Photons	$W\gamma$ at least 1 photon, $W\gamma\gamma$ at least 2 photons
	$p_{\mathrm{T}} > 20$ GeV, $\lvert\eta\rvert < 2.37$, exclude $1.37 < \lvert\eta\rvert < 1.52$
	Tight ID
Combined	$\Delta R_{\gamma,l/\gamma} > 0.4$
	$E_{\mathrm{T}}^{\mathrm{miss}} > 25$ GeV, $m_{\mathrm{T}}^{W} > 40$ GeV
Vetoes	$Z(\gamma) : 80 < m_{l\gamma(\gamma)} < 100$ GeV
	b-jet: $\lvert\eta\rvert < 2.5$

5.2 Template Extraction

The E_{iso} distribution of real photons can be modelled using the double-sided Crystal-Ball function (DSCB) [20] with two additional power-law tails [21]. The extended DSCB function, as illustrated in Figure 17, is characterised by five distinct sections. Each side of the function features two power-law tails with different exponents, m_{i} and n_{i}, with i representing either the left side i=L or the right side i=R. The central region is described by an asymmetric Gaussian distribution with mean μ and widths σ_i. By including a p_{T} dependence for each parameter of the extended DSCB, it is possible to construct the two-dimensional model that is used to derive the generic template $T_{\gamma,j}(E_{\mathrm{iso}}, p_{\mathrm{T}}|\vec{\theta}_{\mathrm{opt}})$, as shown in Equation 9.

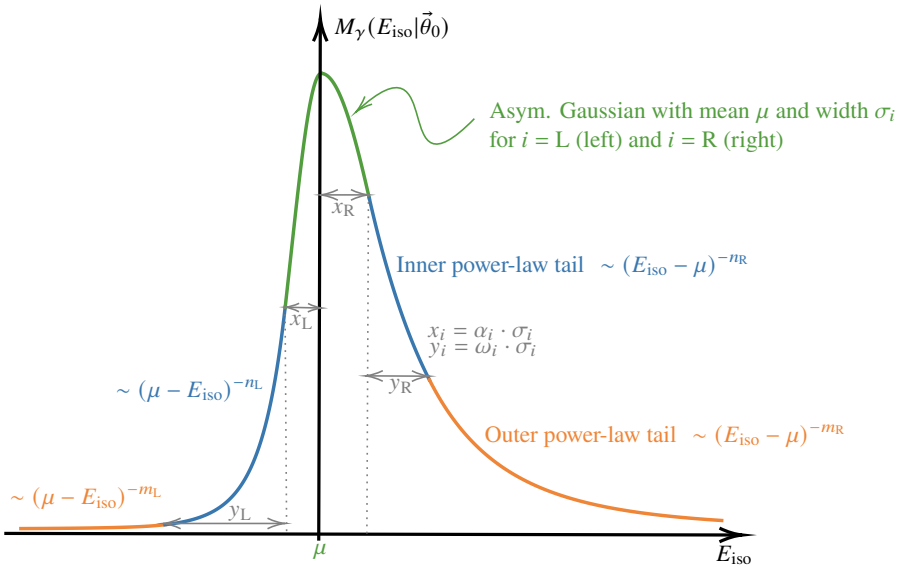

Figure 17: The empirically derived function, double-sided Crystal-Ball function (DSCB) with two power-law tails for modelling the E_{iso} distribution of real photons for a given p_{T} value. The one-dimensional model describing the E_{iso} distribution is referred to as M_γ with the parameters $\vec{\theta}_0$. The function is sectioned into an asymmetric Gaussian distribution with two power-law tails with different exponents on each side. By studying the p_{T} dependence of each parameter of the DSCB function and including them in the model, it is possible to construct the two-dimensional model describing the correlation between E_{iso} and p_{T} [21].

Before the templates are extracted from the final states under Run-3 conditions, the p_{T} dependence of the one-dimensional template M_γ in Run-3 environments is investigated. This is done by performing one-dimensional fits to the E_{iso} distribution for different p_{T} intervals. The parameters show behaviours that can be approximated with either linear or constant p_{T} dependencies, consistent with the observations in [3]. Hence, the same two-dimensional model for the derivation of the generic template for real photons can be used for final states under Run-3 conditions. The approximated p_{T} dependencies of each parameter in the extended DSCB function are shown exemplary for the $W\gamma$ final state in Figure 40 and 41 in Appendix C.

Template Extraction from the $Z\gamma$ Final State

The E_{iso} template for real photon candidates is extracted from $Z\gamma$ MC simulations using the procedure described in Section 4.2. To derive the optimal parameters of the generic template, the extended DSCB with its approximated p_{T} dependence, is fitted to the (E_{iso}, p_{T}) distribution of the leading photon in the $Z\gamma$ final state using a two-dimensional maximum likelihood fit. The exact values of the optimal parameters from the two-dimensional fit can be found in Table 6 in Appendix E. The projections of the two-dimensional template onto

the E_{iso} and p_{T} axes are shown in Figure 18 and 19. The projection in Figure 18 shows good agreement with the E_{iso} distribution. However, there are some discrepancies observed around the peak and inner-right tail in the fit residual (lower panel). These inaccuracies are likely because the model used for the two-dimensional distribution of (E_{iso}, p_{T}) is derived empirically. The extended DSCB model and its approximated p_{T} dependence do not fully account for all physical effects. The template extraction fit for the $Z\gamma$ final state under Run-2 conditions exhibits smaller deviations than under Run-3 conditions. This is likely due to the fact that the MC simulations used in this case offer higher statistics compared to those used for the Run-2 analysis. With higher statistics the inaccuracies of the empirical model get more significant due to the smaller statistical uncertainties. This observation suggests that there are systematic limitations to the empirically derived model for the $(E_{\text{iso}}, p_{\text{T}})$ distribution when dealing with very high statistics.

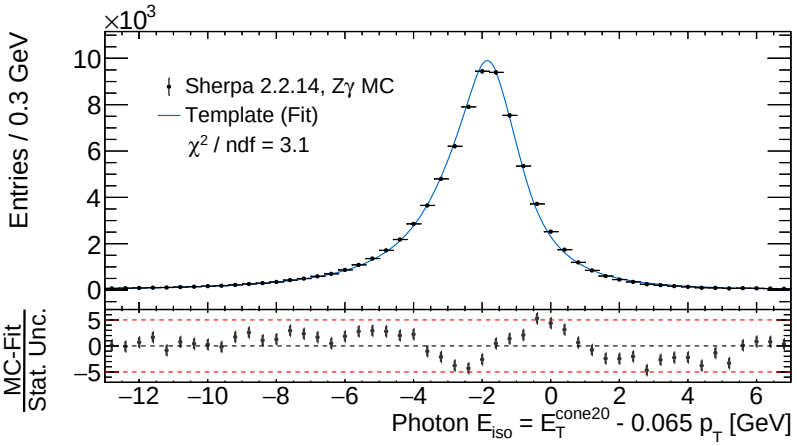

Figure 18: The template extraction from $Z\gamma$ Run-3 MC simulations. The projection of the two-dimensional fit onto the E_{iso} axis is shown. The template shows good agreement with the E_{iso} distribution. Some systematic trends are seen in the fit residual around the peak and inner-right tail regions.

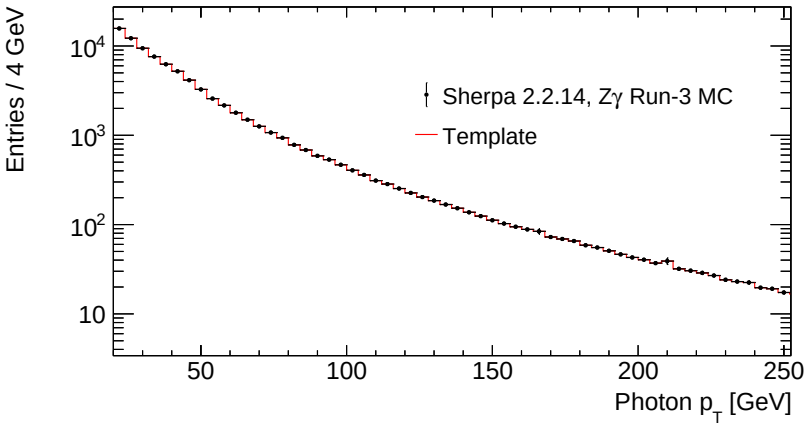

Figure 19: The two-dimensional template projected onto the p_{T} axis, modelled with a binned histogram.

Template Extraction from the $W\gamma$ Final State

The generic template for real photons is re-extracted from the $W\gamma$ process to enable a comparison between the two templates and to examine their individual applicability to other final states. The two-dimensional fit projection onto the E_{iso} and p_{T} axis are presented in Figure 20 and 21. The values of the optimal parameters from the two-dimensional fit can be found Table 7 in Appendix E. The template shows improved agreement with the E_{iso} distribution, with respect to the $Z\gamma$ final state, as observed in the fit residual and lower χ^2_{red} value. Still, small trends are observed in the fit residual around the inner-right tail. Given that the $W\gamma$ final state offers similarly high statistics as the $Z\gamma$ final state, these differences might suggest that the empirical model describes the $(E_{\text{iso}}, p_{\text{T}})$ distribution of the photon in the $W\gamma$ final state more accurately than that of the $Z\gamma$ final state.

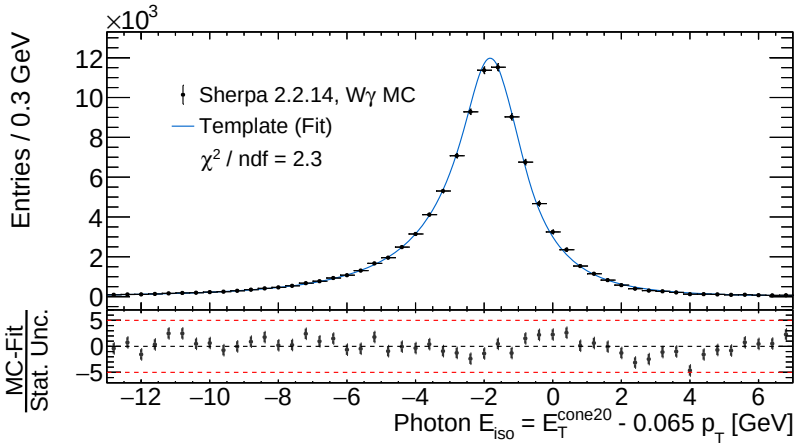

Figure 20: The template for real photon candidates extracted from the $W\gamma$ final state. The graph shows the projection of the two-dimensional fit onto the E_{iso} axis. As seen in the fit residual, the template shows only small systematic deviations around the inner-right tail.

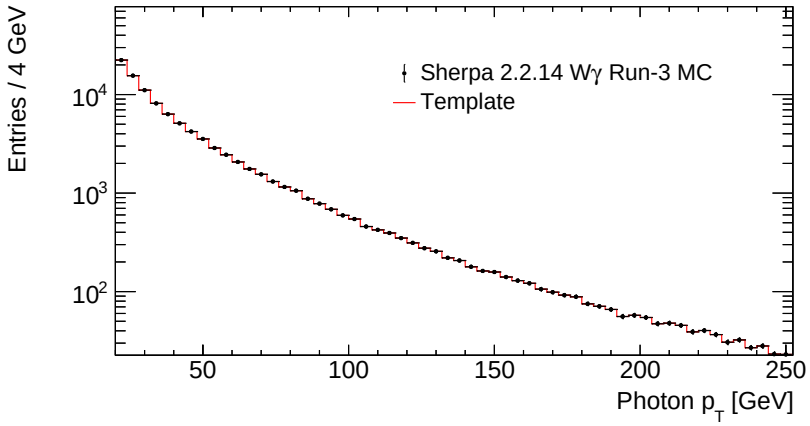

Figure 21: The two-dimensional template projected onto the p_{T} axis, modelled with a binned histogram.

5.3 Transfer to Different Final States

In this section, the above extracted templates from the $Z\gamma$ and $W\gamma$ final states will be compared to the $W\gamma\gamma$ and $Z\gamma\gamma$ final states and finally to each other. The comparisons of the templates for real photons performed in this thesis are summarised in Figure 22.

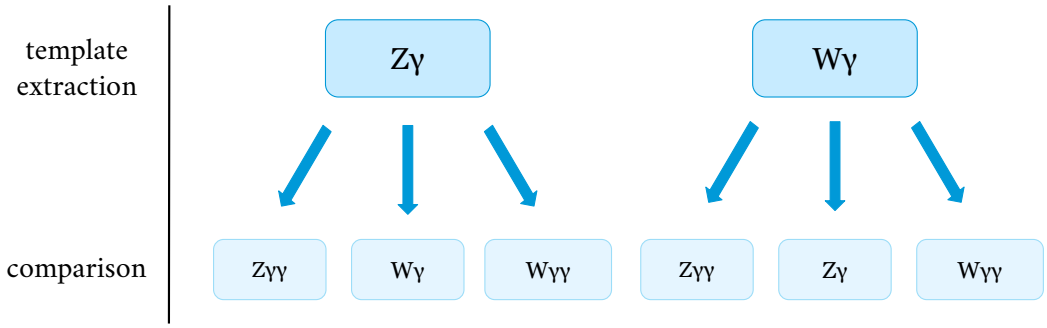

Figure 22: Overview of all comparisons for real photons in this analysis. The optimal parameters for the templates are extracted from the high statistics $Z\gamma$ and $W\gamma$ final states. Without performing a fit, the templates are applied to other final states (bottom row in illustration) by multiplying the generic template with the corresponding p_{T} distribution.

First, the two templates extracted from the $Z\gamma$ and $W\gamma$ process (from now on referred to as the $Z\gamma$ and $W\gamma$ template) are applied to the E_{iso} distribution of the leading photon in the $Z\gamma\gamma$ final state. For the comparisons, no fit is necessary; only the generic $Z\gamma$ and $W\gamma$ templates are multiplied by the corresponding p_{T} distribution of the final state photon, respectively. The same comparison is done for the $W\gamma\gamma$ final state. Additionally, the differences in the templates extracted from the $Z\gamma$ and $W\gamma$ final states are investigated.

$Z\gamma$ and $W\gamma$ Template Comparison to the $Z\gamma\gamma$ Final State

The templates are applied to the E_{iso} distribution of the leading photon in the $Z\gamma\gamma$ final state. To enable a comparison of the $Z\gamma$ and $W\gamma$ templates, they are displayed in the same Figure 23 with different colours, red dashed and blue solid. As observed in the figure, both templates give an accurate description of the E_{iso} distribution. No systematic deviations can be observed in the fit residual. Moreover, the $Z\gamma$ and $W\gamma$ templates also show good agreement with the E_{iso} distributions of the subleading photon and a combination of the two photons. These comparisons, together with the corresponding projections onto the p_{T} axes are presented in Appendix E.

It is notable in Figure 23 that the shapes of the $Z\gamma$ template (dashed red) and $W\gamma$ template (blue solid) are almost identical and the systematic trends seen in the fit residuals are very similar. Within the uncertainties of the E_{iso} distribution, the templates are equivalent. The systematic trends seen in the fits for the individual template extraction from the $Z\gamma$ and $W\gamma$ final state are not visible in the comparisons with the $Z\gamma\gamma$ final state. This is likely due to the fact that the $Z\gamma\gamma$ final state offers significantly lower statistics than the $Z\gamma$ and $W\gamma$ final states. With such statistics, the deviations emerging from inaccuracies of the model are not significant.

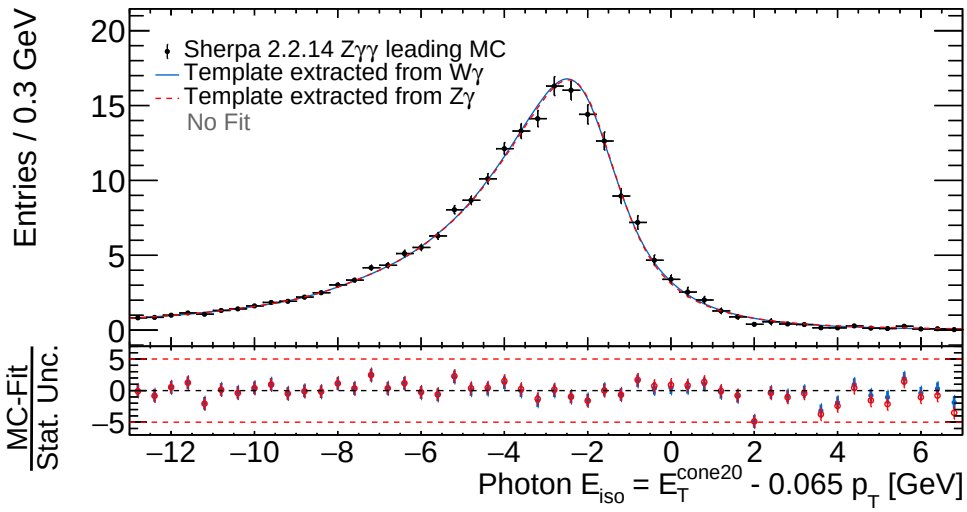

Figure 23: The templates with optimal parameters extracted from the $Z\gamma$ (dashed red line) and $W\gamma$ (solid blue line) final states applied to the E_{iso} distributions of the $Z\gamma\gamma$ final state's leading photon. No fit is performed, only the two-dimensional template is projected onto the E_{iso} axis. The templates show good agreement with E_{iso} distribution and no significant deviation is observed. The templates describe the distribution equally well and are equivalent within the uncertainties of the distribution.

$Z\gamma$ and $W\gamma$ Template Comparison to the $W\gamma\gamma$ Final State

The comparison of the $Z\gamma$ and $W\gamma$ templates to the E_{iso} distribution of the leading photon in the $W\gamma\gamma$ final state is performed analogously as for the $Z\gamma\gamma$ final state and is depicted in Figure 24. Also here, the templates describe the E_{iso} distribution of the $W\gamma\gamma$ final state's leading photon remarkably well. There are no significant systematic trends observed in the fit residuals. Further comparisons to subleading photon's and a combination of both photons' E_{iso} distributions show similar results, as can be seen in Appendix E.

Just like for the comparison with the $Z\gamma\gamma$ final state, the two templates almost perfectly align and are equally suitable for the description for the E_{iso} distribution of the leading $W\gamma\gamma$ final state photon.

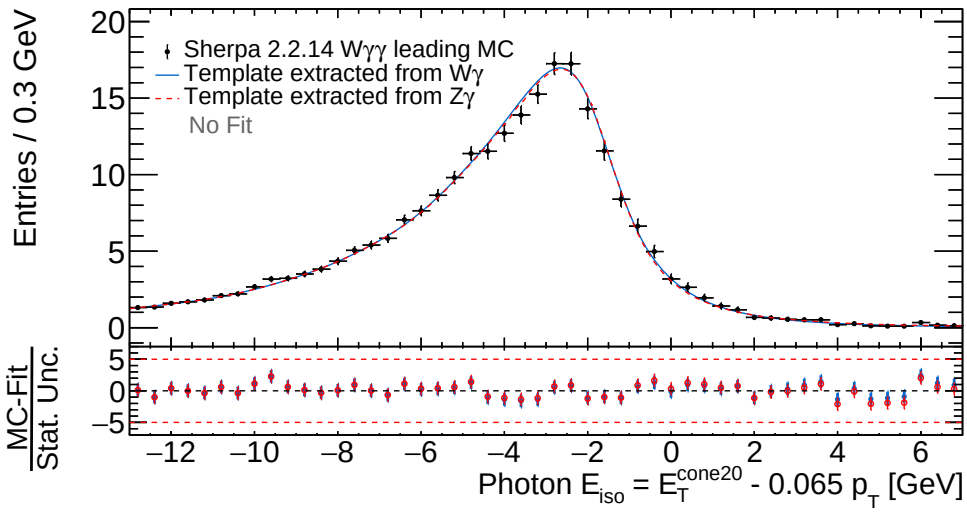

Figure 24: The templates for real photons derived from the $Z\gamma$ (dashed red line) and $W\gamma$ (solid blue line) final states compared to the E_{iso} distribution of the leading photon in the $W\gamma\gamma$ final state. There is good agreement observed with the E_{iso} distribution for both templates. The fit residuals reveal no systematic trends. The templates are equivalent within the uncertainties of the E_{iso} distribution.

Comparison of the $W\gamma$ and $Z\gamma$ Templates

Finally, the extracted templates from $W\gamma$ and $Z\gamma$ are compared to each other. Both the template extracted from the $Z\gamma$ and from the $W\gamma$ final state is applied to the $W\gamma$ MC simulations and vice versa. Figure 25 shows the template extraction from the $Z\gamma$ final state (dashed red line) and the $W\gamma$ template (solid blue line) applied to the same final state. The $W\gamma$ template describes the E_{iso} distribution well, and the trends seen in the fit residuals closely resemble those observed in the template extraction. This affirms that the discrepancies between the $W\gamma$ template and the E_{iso} distribution emerge mainly from the systematic inaccuracies of the empirical model and not from differences between the two template shapes.

As can be seen in the fit residual in Figure 25, the shapes of the $Z\gamma$ and $W\gamma$ template exhibit only very small differences around the peak and the inner-right tail. These deviations are possibly due to differences between the $Z\gamma$ and $W\gamma$ final states, such as the amount of ISR and FSR events, which also influence the E_{iso} distribution [21]. Nevertheless, the deviations are within the same trends and balance each other out, in such a way that both templates still describe the E_{iso} distributions of the two different final states equally well.

Similar observations are done for the analogue comparison of the $Z\gamma$ template with the $W\gamma$ final state, shown inn Figure 26. Here, the templates show even less differences to each other with respect to the previous comparison in Figure 25.

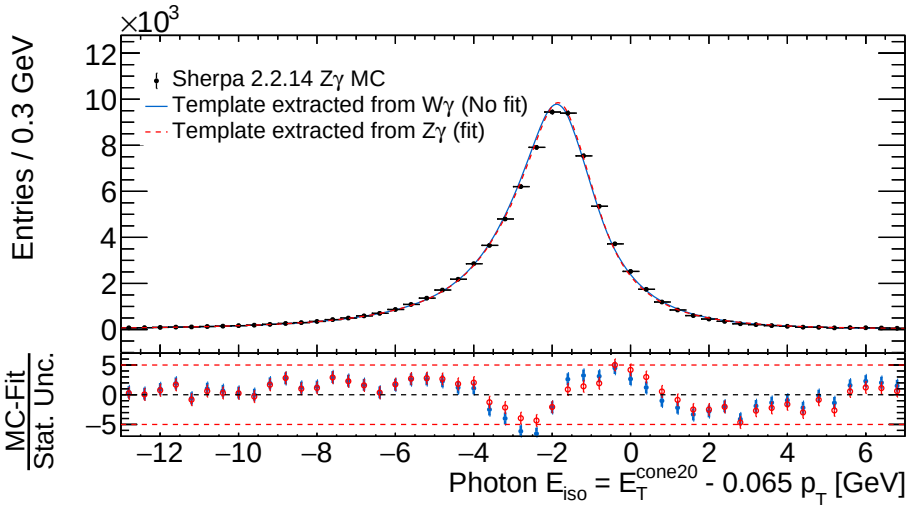

Figure 25: The template extracted from the $Z\gamma$ and $W\gamma$ final states applied to the E_{iso} distribution of the leading photon in the $Z\gamma$ final state. The templates describes the distribution well. The systematic trends observed in the fit residual of the $W\gamma$ template closely resembles the trends of extraction template from $Z\gamma$ MC simulations. This indicates that the systematic trends mainly emerge from the inaccuracies of the model. Small differences between the templates are seen in the trends around the peak and inner-right tail.

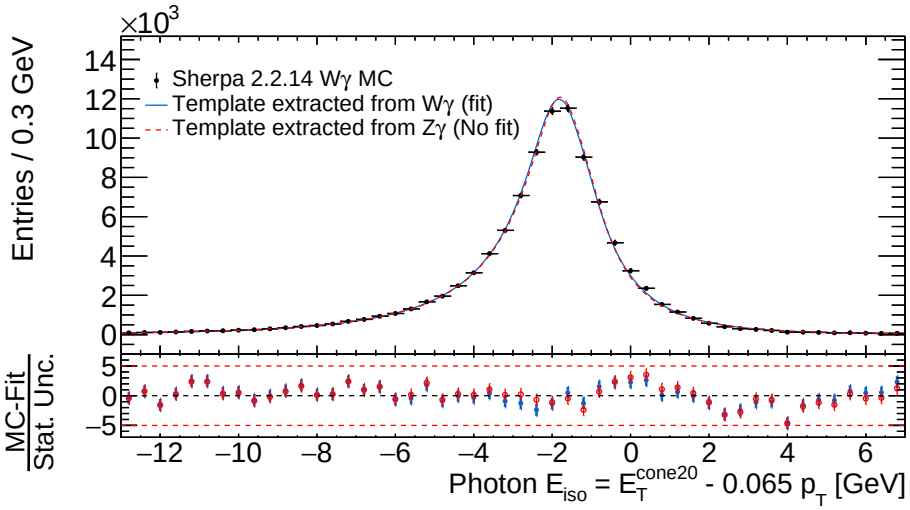

Figure 26: The template extracted from the $Z\gamma$ and $W\gamma$ final states applied to the $W\gamma$ final state. The templates show good agreement with the distribution and the systematic trends observed in the fit residual are very similar, affirming that the templates describe the distribution equally well. The applied $Z\gamma$ template is only limited by the systematic inaccuracies of the model.

The various comparisons performed in this chapter strongly indicate that the Enhanced Template Fit Method can be applied to the E_{iso} distributions of real photons in various final states under Run-3 conditions. Furthermore, it was proven that the Enhanced Template Fit Method for real photons can be employed to final states with W bosons. Both templates for real photons extracted from the $Z\gamma$ and $W\gamma$ final states most likely correspond to universal templates and can be used to describe the E_{iso} distribution of real photons in other final states without having to execute a fit procedure.

Systematic trends observed in the fit residuals of the template extractions (Figures 18 and 20) suggest that the empirically derived model for correlation between E_{iso} and p_{T} does not fully account for all physical effects. Nevertheless, for the comparisons to final states like $Z\gamma\gamma$ and $W\gamma\gamma$ Run-3 MC simulations offering lower statistics, the observed systematic variations are negligible. The systematic limitation of the model does not hinder the application of the Enhanced Template Fit Method on data. This is because ATLAS Run-3 data in one of the considered final states is expected to have significantly lower statistics compared to the corresponding MC simulations. Specifically, in this analysis, the $Z\gamma$ final state in data is expected to have around 0.5 % of the statistics of its MC counterpart, while the $W\gamma$ final state has about 9 %. The expected statistics for data are similar to or lower than those of the $Z\gamma\gamma$ and $W\gamma\gamma$ MC simulations, where no systematic deviations are observed. Another reason the systematic limitation of the model do not hinder the application on ATLAS Run-3 data, is that the fake contribution to the background is estimated via integration of the template from $-\infty$ to 0. The value for the integral can still be close to the real value, despite the potential imperfections of the template.

6 Templates for Fake Photon Candidates

The following chapter investigates the templates for fake photon candidates. The templates are extracted from Z+jets and W+jets MC simulations. Similar to the real photons, the templates are extracted from these MC simulations since they offer significantly higher statistics than the other studied final states with fake photons. Furthermore, the templates are compared to each other, as well as to the $Z\gamma\gamma$ and $W\gamma\gamma$ final states.

6.1 Event Selections

A fake-enhanced selection is performed on Z+jets and W+jets MC samples to select $Z\gamma$ and $W\gamma$ final states with the leading photon being a fake photon produced in jet fragmentations. To differentiate them from the final states with real photons, they are referred to as Zj and Wj, with j corresponding to a fake photon. Since the relevant Zj and Wj final states are those contributing to the background of the $Z\gamma$ and $W\gamma$ final states, the corresponding event selections are comparable. The Zj and Wj events are selected using the same selection criteria as listed in Table 2 and 3. Unlike the real photons, the fake photons are required to fail the tight ID but still satisfy a looser ID WP. The applied criteria for the truth match is disregarded in the selection of fake photons. The fake enriched selection of $Z\gamma\gamma$ and $W\gamma\gamma$ final states with one real and one fake photon are performed similarly with $Z\gamma$+jets and $W\gamma$+jets MC samples. These event selections are referred to as $Zj\gamma$, $Z\gamma j$, $Wj\gamma$ and $W\gamma j$ selections.

6.2 Template Extraction

The E_{iso} distribution of fake photons was found to be well-modelled by the Bukin NovosibirskA function [22]. The function is separated into three regions, as illustrated in Figure 27. The right and left sides of the function are described by exponential tails with variables ρ_{R} (right side) and ρ_{L} (left side) factorised in the exponent. The middle section takes an asymmetric peak shape, with peak position μ, width σ and asymmetry ξ.

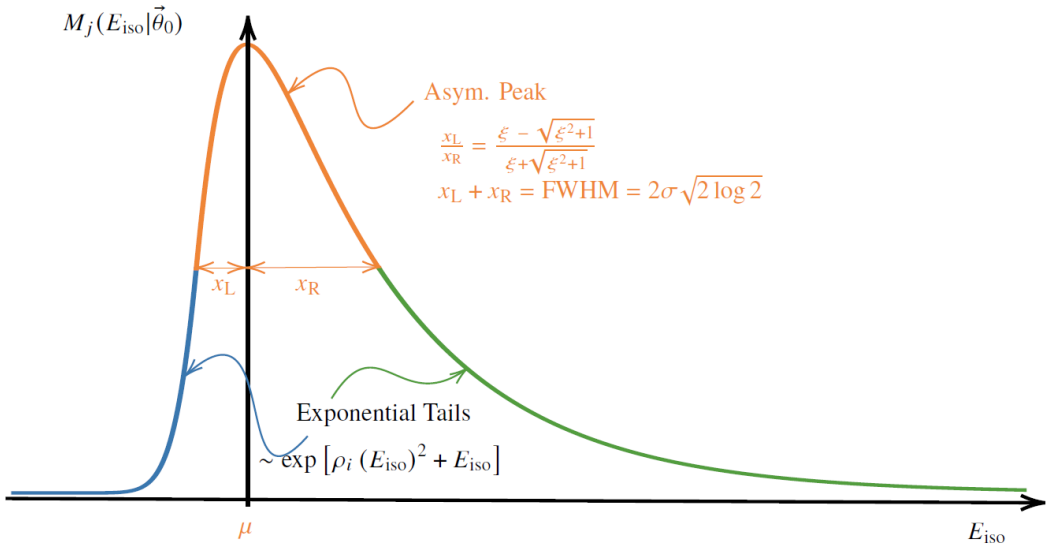

Figure 27: The Bukin NovosibirskA function is used to model the E_{iso} distribution of fake photons. M_j represents the one-dimensional model describing the E_{iso} distribution for a given value of p_{T}. The function features an asymmetric peak at position μ and asymmetry ξ. The width of the asymmetric peak is characterised by the variable σ, with FWHW $= \sqrt{2\log(2)} \cdot \sigma$. Each side of the peak is described by an exponential tail with different exponents. The exponents are characterised by the variables ρ_i with $i = \text{L}$ for the left side and $i = \text{R}$ for the right side. Taken from [3].

Analogue to the real photons, the p_{T} dependence of the one-dimensional E_{iso} template is approximated by studying the individual p_{T} dependence of each parameter of the Bukin NovosibirskA model. By including the p_{T} dependent parameters in the model, a two-dimensional model can be constructed that describes the correlation between E_{iso} and p_{T}.

Template Extraction from the Zj and Wj Final States

The E_{iso} templates for fake photons are derived from the Zj and Wj final states with the same procedure as described in Section 4.2. In the MC simulations for Zj final states, there is a significant amount of additional objects in the electron decay channel misidentified as photons. For this reason, the template from the Zj final state is only extracted from the muon decay channel. This is expected to have no effect on the shape of the isolation template, since only ISR events are selected, where the final state leptons do not interact with the photon. The isolation templates are obtained by projecting the two-dimensional fit results onto the E_{iso} axis respectively, as shown in Figure 28 and 29. The projections onto the p_{T} axis can be found in Appendix E in Figure 56 and 57.

The template extracted from $Z(\rightarrow \mu\mu)$+jets MC simulations in Figure 28 provides a good description of the E_{iso} distribution. However, small deviations around the tails can be observed in the fit residual. Analogue to the templates for real photons, the inaccuracies are likely due to the fact that the model is derived empirically and its p_{T} dependence is approximated. Therefore the extracted templates do not describe all physical effects entirely. Similar to the real photons, the template extraction from the W+jets MC simulations in Figure 29 shows better agreement than the extraction from the $Z(\rightarrow \mu\mu)$+jets MC simulations. This is can be seen in the fit residual that shows no systematic discrepancies.

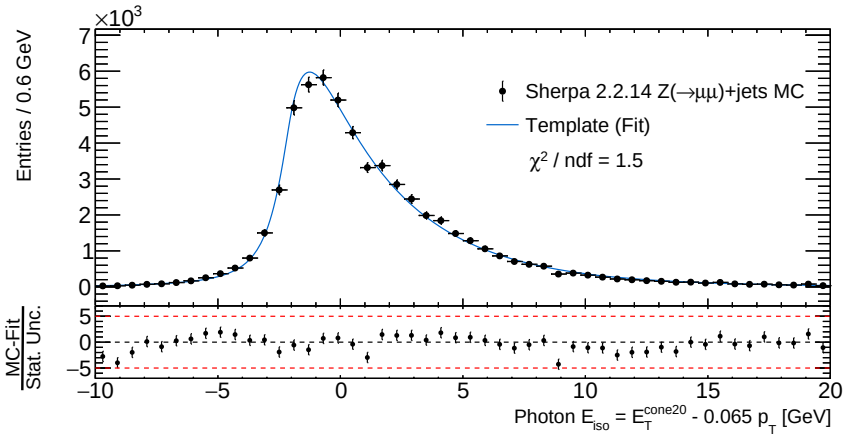

Figure 28: Template for fake photons extracted from $Z(\rightarrow \mu\mu)$+jets MC simulations with a two-dimensional fit. The template is obtained by projecting the two-dimensional fit onto the E_{iso} axis. The template shows small deviations around the tails, as observed in the fit residual. Nevertheless, the χ^2_{red} value indicates good agreement between the template and the E_{iso} distribution.

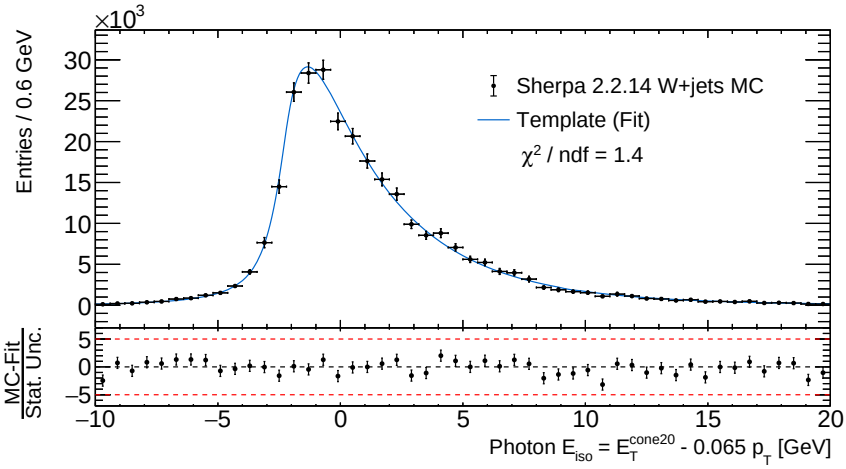

Figure 29: Template extraction from W+jets MC simulations. The template is obtained by projecting the two-dimensional fit onto the E_{iso} axis. No systematic trends are observed in the fit residual and the χ^2_{red} value indicates good agreement between the template and the E_{iso} distribution.

6.3 Transfer to Different Final States

The applicability of the two templates for fake photons to other final states is investigated. All the comparisons performed with the templates for fake photons are summarised in Figure 30.

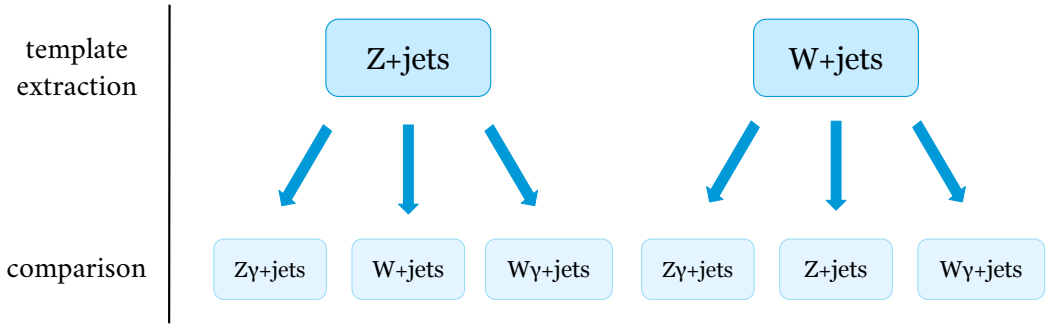

Figure 30: Overview of all comparisons with the templates for fake photons in this thesis. The optimal parameters for the templates are extracted from the high statistic Zj and Wj final states. Without performing a fit, the templates are compared to other final states (bottom row in illustration) by multiplying the generic template with the corresponding p_{T} distribution of the fake photon in the final state.

Template Comparison to $Z\gamma$+jets and $W\gamma$+jets

The templates for fake photon candidates extracted from Z+jets and W+jets MC simulations (from now referred to as the Zj and Wj template) are compared to the E_{iso} distribution of $Z\gamma$+jets and $W\gamma$+jets MC simulations. At first, the templates are applied to the E_{iso} distribution of a combination of the fake photons in the $Zj\gamma$ and $Z\gamma j$ final states. The comparison is showed in Figure 31. The corresponding projection of the templates onto the p_{T} axes are shown in Figure 58 in Appendix E. To enable a comparison of the Zj and Wj templates, they are displayed in the same Figure 31 with different colours, red dashed and blue solid. Both templates show overall good agreement within the uncertainty of the E_{iso} distributions. However, some systematic deviations are seen in the fit residual around the right tail of the distribution. The residual value of the data points in this region are not visible since the fit residual is set to a range [-5,5] for visualisation purposes. The deviations are caused by the very small statistical uncertainties in this specific region leading to large deviations. The large uncertainties of the E_{iso} distribution observed

around the peak position, can be explained by the low statistic of the $Zj\gamma$ and $Z\gamma j$ final states.

Furthermore, it can be seen in Figure 31 that the two templates have almost identical shapes and the systematic discrepancies as seen in the fit residuals show very similar trends. This implies that it does not make a difference whether the E_{iso} distribution from $Z\gamma$+jets MC simulations is described by the template extracted from Z+jets or the templates extracted from W+jets MC simulations.

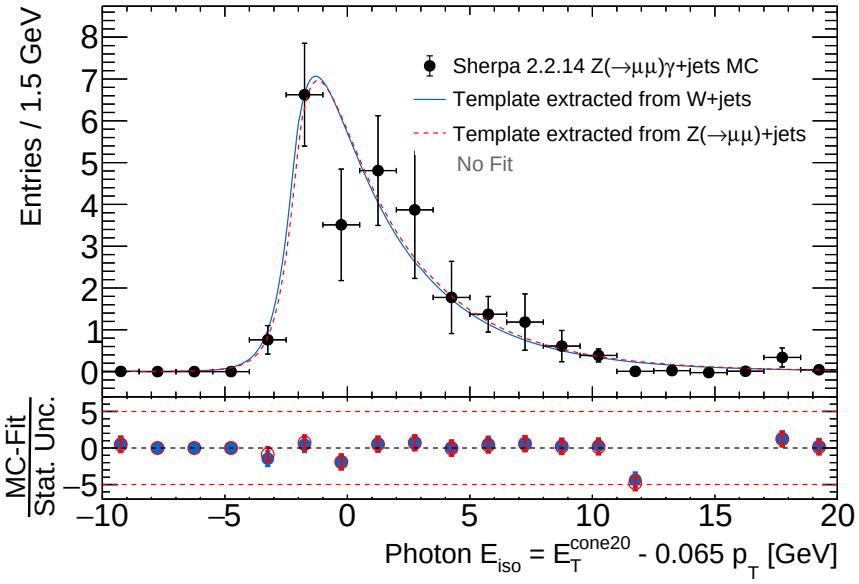

Figure 31: The templates extracted from Z+jets and W+jets MC simulations applied to the E_{iso} distribution of a combination of the fake photons in the $Zj\gamma$ and $Z\gamma j$ final states from the muon decay channel. Even though no fit is performed, both templates describe the distribution well. Some data points around the right tail are not visible in the fit residual due to deviations larger than 5σ. The Zj and Wj templates are equivalent within the uncertainties of the distribution.

Moreover, the templates are applied to the E_{iso} distribution of the fake photons produced in $Wj\gamma$ and $W\gamma j$ final states. The comparison is depicted in Figure 32. The observations are similar to those made in the $Z\gamma$+jets comparison. The Zj and Wj templates describe the E_{iso} distribution accurately and are equivalent to each other within the uncertainties of the E_{iso} distribution. Unlike the previous comparison with $Z\gamma$+jets MC simulations, no deviations are observed around the right tail, whereas small deviations are seen around the left tail in the fit residual. This suggests that the deviations are a feature of the $Z(\rightarrow \mu\mu)$+jets MC simulations.

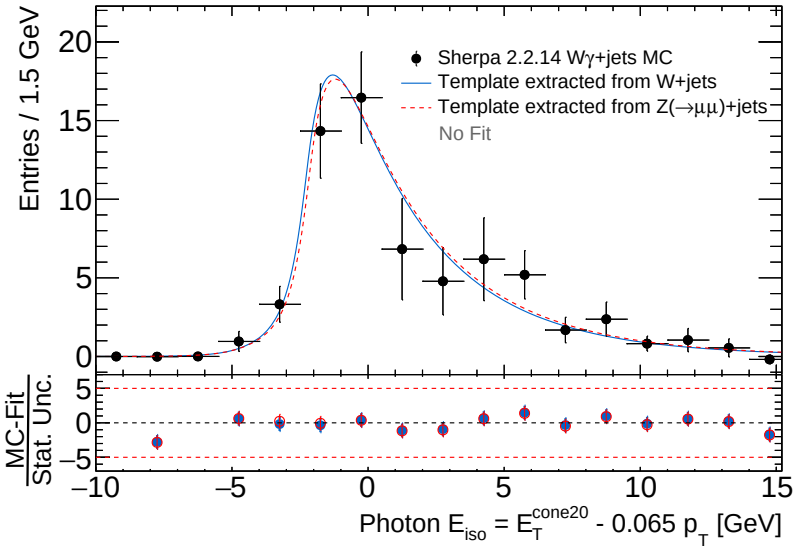

Figure 32: The templates extracted from Z+jets and W+jets MC simulations applied to the E_{iso} distribution of a combination of the fake photons in the $Wj\gamma$ and $W\gamma j$ final states. Despite the fact that no fit was performed, the templates show good agreements with the E_{iso} distribution. Only small deviations are observed around the left tail. The templates are equivalent within the uncertainties of the distribution.

In general, the observations in both comparisons support the generalisation of the templates for fake photons in the Enhanced Template Fit Method in Run-3 environments.

Comparison of Z+jets and W+jets Templates

The templates extracted from the W+jets and Z+jets MC simulations are compared to each other. Figure 33 shows the template extraction from the Zj final state (red dashed line) together with the Wj template (blue solid line). The Wj template is applied to the distribution from the Zj final state without performing a fit, just like for the previous comparisons.

It is notable in Figure 33, that the systematic trends seen in the template extraction from the Zj process are almost identical to the deviations of the Wj template to the E_{iso} distribution. This shows that the Wj template describes the E_{iso} distribution as accurately as possible considering the systematic discrepancies caused by inaccuracies of the empirical model. The same observation is made in Figure 34 showing the analogue comparisons to the Wj final state. Also here, the applied Zj template shows no more discrepancies than those emerging from the inaccuracy of the model itself. Regardless, the statistics in the Z+jets and W+jets MC simulations are notably higher than the expected statistics of fake photons

in proton-proton collision data. For this reason, the systematic deviations caused by the inaccuracies of the model for fake photons will most likely be insignificant when applying the Enhanced Template Fit Method to Run-3 data. Together, the comparisons strongly

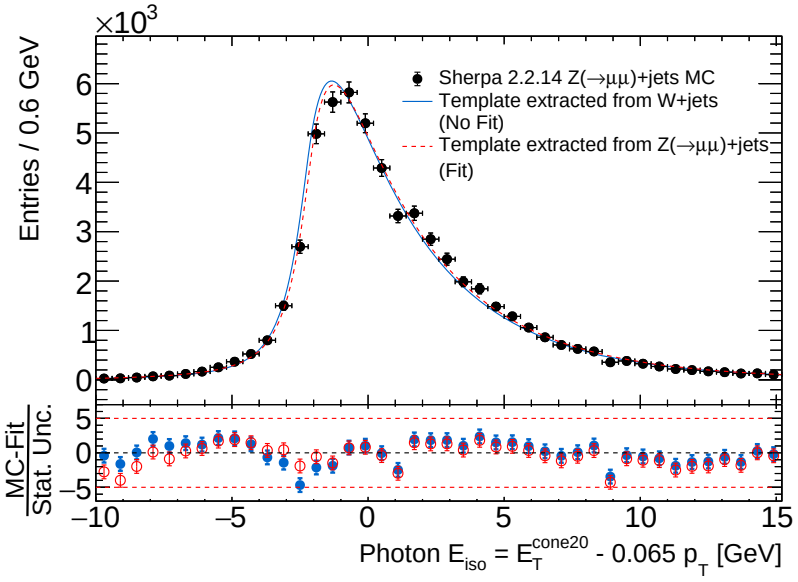

Figure 33: The template extraction in the Zj process (red dashed line) together with the Wj template (blue solid line) applied to the E_{iso} distribution of the fake photon in the Zj final state. The deviations of the templates seen in almost identical trends in the fit residuals as the fitted template. The applied template is therefore only limited by the inaccuracies of the empirical model and those not show any additional discrepancies.

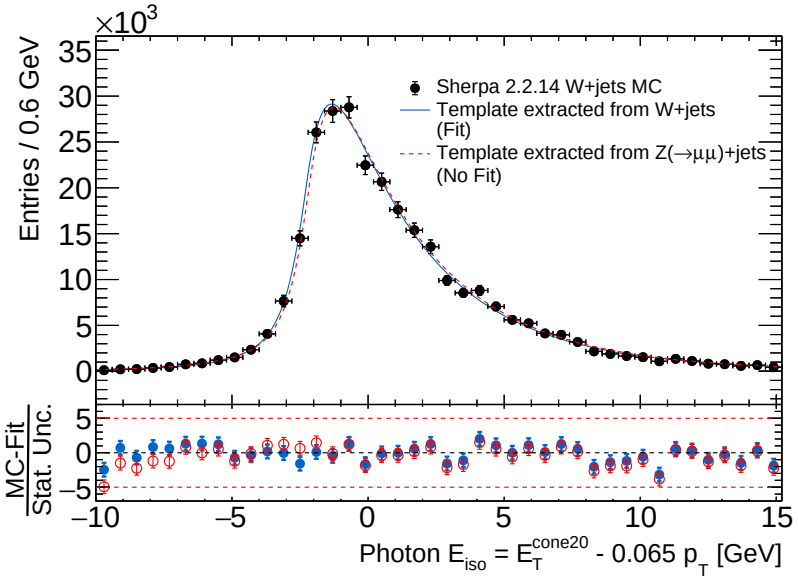

Figure 34: The template extraction in the Wj process (blue solid line) together with the Zj template (dashed red line) applied to the E_{iso} distribution of the fake photon in the Wj final state.

indicate that both templates for fake photons represent universal isolation templates and that the Enhanced Template Fit Method can be extended to final states with W bosons for fake photons.

7 Conclusion

To apply the Template Fit Method to other final states it is necessary to extract new templates, due to their strong p_{T} dependence. This challenge was addressed in a previous ATLAS study [3] with Run-2 data by developing a new Enhanced Template Fit Method. The template was generalised by separating the template into a generic part, describing the correlation between E_{iso} and p_{T}, and the final state-dependent p_{T} distribution. The analysis in this thesis accesses the applicability of the Enhanced Template Fit Method to Run-3 environments and studies its potential extension to final states with W bosons.

In the analysis, new templates for final states under Run-3 conditions are extracted due to the pile-up dependence of the E_{iso} distribution. Since pile-up differs between Runs, it is essential to extract new templates for both real and fake photons. Before applying the same two-dimensional models to extract templates from final states under Run-3 conditions, the p_{T} dependence of the one-dimensional models for the E_{iso} distributions of real and fake photons is investigated. This p_{T} dependence is studied by fitting the one-dimensional models to E_{iso} distributions for different p_{T} intervals. The obtained templates for real and fake photons exhibit similar p_{T} dependencies to those observed in the study of final states under Run-2 conditions. Consequently, the same two-dimensional models describing the correlation between E_{iso} and p_{T} can be applied to Run-3 final states to derive the optimal parameters for the generic part of the isolation energy template for real and fake photons.

The new templates for real and fake photons are extracted from the final states offering the highest statistics, namely the $Z\gamma$, $W\gamma$, Zj and Wj final states. The derived templates describe the corresponding E_{iso} distribution accurately. However, small systematic deviations are observed in the individual fit residuals for both real and fake photons. This observation suggests that the models for the $(E_{\mathrm{iso}}, p_{\mathrm{T}})$ distributions have an underlying inaccuracy. This is anticipated, since the model is only empirically derived and therefore likely does not fully account for all physical effects. Nevertheless, these deviations are only significant for very high statistics MC simulations. The deviations do not hinder the implementation of the Enhanced Template Fit Method in Run-3 environments. This is because ATLAS Run-3 data is expected to have much lower statistics, making these systematic deviations negligible compared to the statistical uncertainties.

To examine the generalisation of the templates, they are compared to other final states, such as $Z\gamma\gamma$, $W\gamma\gamma$, $Z\gamma$+jets, and $W\gamma$+jets. To apply the templates to another final state, the extracted generic templates are multiplied by the corresponding p_{T} distribution. The two-dimensional template is projected onto the E_{iso} axis and compared to the E_{iso} distribution of the final state. The templates for both real and fake photons show good agreements with the E_{iso} distribution across the different final states, despite the fact that no fit is performed. This supports the possible application of the Enhanced Template Fit Method to final states under Run-3 conditions.

Furthermore, the differences of the templates for real photons extracted from the $Z\gamma$ and $W\gamma$ final states are studied. The two templates are compared by applying both templates to the E_{iso} distribution of the same final state. In these comparisons, the templates show almost identical systematic deviations. This strongly indicates that the discrepancies emerge from the inaccuracies of the empirical model and not from differences between the two templates. The two templates for real photons are equivalent within the uncertainties of the distributions with the statistics of the used MC simulations and both can be used to describe the E_{iso} distributions. This shows that the Enhanced Template Fit Method for real photons can be extended to final states with W bosons.

The same comparisons are performed for the templates for fake photons. In the comparisons with final states offering lower statistics, such as $Zj\gamma$ and $Wj\gamma$ the templates are equivalent within the uncertainties of the E_{iso} distributions. For the cross comparisons of the final states offering high statistics, the templates show small additional systematic deviations to the expected deviations caused by the inaccuracy of the two-dimensional model. This indicates small discrepancies between the template extracted from Z+jets and from W+jets MC simulations. These discrepancies are likely caused by small differences between the $Z\gamma$ and $W\gamma$ final states, such as the amounts of ISR and FSR events. Yet, for the statistics expected in proton-proton collision data, these differences are expected to be negligible.

With these results it is strongly suggested that the Enhanced Template Fit Method can be successfully implemented under Run-3 conditions, including final states with W bosons.

Appendix

A Shower Shape Variables and ID Criteria

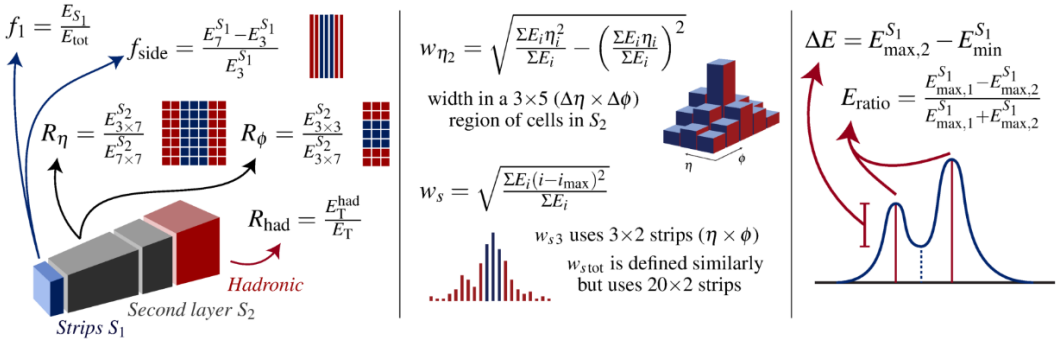

Figure 35: Definition of the photon identification discriminating shower shape variables. $E_{\text{C}}^{\text{S}_N}$ represents the electromagnetic energy collected in the N-th longitudinal layer of the electromagnetic calorimeter in a cluster of properties C, identifying the number and/or properties of selected cells. E_i is the energy in the i-th cell, and η_i is the pseudorapidity centre of the cell. Taken from [23].

A Shower Shape Variables and ID Criteria

Table 4: Selection cuts on shower shape variables for different ID criteria. Taken from [14].

Category	Description	Name	*loose*	*tight*
Acceptance	$\|\eta\| < 2.37$, with $1.37 \leq \|\eta\| < 1.52$ excluded	-	✓	✓
Hadronic leakage	Ratio of E_T in the first sampling layer of the hadronic calorimeter to E_{T} of the EM cluster (used over the range $\|\eta\| < 0.8$ or $\|\eta\| > 1.52$)	R_{had1}	✓	✓
	Ratio of E_{T} in the hadronic calorimeter to $E_{\mathbf{T}}$ of the EM cluster (used over the range $0.8 < \|\eta\| < 1.37$)	R_{had}		✓
EM middle layer	Ratio of the energy in $3 \times 7\, \eta \times \phi$ cells over the energy in 7×7 cells centered around the photon cluster position	R_η	✓	✓
	Lateral shower width, $\sqrt{\langle \Sigma E_i \eta_i^2 \rangle / \langle \Sigma E_i \rangle - (\langle \Sigma E_i \eta_i \rangle / \langle \Sigma E_i \rangle)^2}$, where E_i is the energy and η_i is the pseudorapidity of cell i and the sum is calculated within a window of 3×5 cells	w_{η_2}		✓
	Ratio of the energy in $3 \times 3\, \eta \times \phi$ cells over the energy of 3×7 cells centered around the photon cluster position	R_ϕ		✓
EM strip layer	Lateral shower width, $\sqrt{\Sigma E_i (i - i_{\max})^2 / \Sigma E_i}$, where i runs over all strips in a window of $3 \times 2\, \eta \times \phi$ strips, and $i_{\max}$ is the index of the highest-energy strip calculated from three strips around the strip with maximum energy deposit	w_{s3}		✓
	Total lateral shower width $\sqrt{\Sigma E_i (i - i_{\max})^2 / \Sigma E_i}$, where i runs over all strips in a window of $20 \times 2\, \eta \times \phi$ strips, and $i_{\max}$ is the index of the highest-energy strip measured in the strip layer	w_{stot}		✓
	Energy outside the core of the three central strips but within seven strips divided by energy within the three central strips	f_{side}		✓
	Difference between the energy associated with the second maximum in the strip layer and the energy reconstructed in the strip with the minimum value found between the first and second maxima	ΔE_s		✓
	Ratio of the energy difference between the maximum energy deposit and the energy deposit in the secondary maximum in the cluster to the sum of these energies	E_{ratio}		✓
	Ratio of the energy in the first layer to the total energy of the EM cluster	f_1		✓

B MC Simulations

Sample	DSID	Generator	Run
Z(ee)γ_pty_15_35	366141	Sherpa 2.2.4	Run-2
Z(ee)γ_pty_35_70	366142	Sherpa 2.2.4	Run-2
Z(ee)γ_pty_70_140	366143	Sherpa 2.2.4	Run-2
Z(ee)γ_pty_140_E_CMS	366144	Sherpa 2.2.4	Run-2
Z($\mu\mu$)γ_pty_15_35	366146	Sherpa 2.2.4	Run-2
Z($\mu\mu$)γ_pty_35_70	366147	Sherpa 2.2.4	Run-2
Z($\mu\mu$)γ_pty_70_140	366148	Sherpa 2.2.4	Run-2
Z($\mu\mu$)γ_pty_140_E_CMS	366149	Sherpa 2.2.4	Run-2
$Z(ee)\gamma$	700770	Sherpa 2.2.14	Run-3
$Z(\mu\mu)\gamma$	700771	Sherpa 2.2.14	Run-3
$W(e\nu)\gamma$	700773	Sherpa 2.2.14	Run-3
$W(\mu\nu)\gamma$	700774	Sherpa 2.2.14	Run-3
$W(e\nu)\gamma\gamma$	700870	Sherpa 2.2.14	Run-3
$W(\mu\nu)\gamma\gamma$	700871	Sherpa 2.2.14	Run-3
$Z(ee)\gamma\gamma$	700873	Sherpa 2.2.14	Run-3
$Z(\mu\mu)\gamma\gamma$	700874	Sherpa 2.2.14	Run-3
$W(e\nu)$ + jets [BFilter]	700777	Sherpa 2.2.14	Run-3
$W(e\nu)$ + jets [CFilter,BVeto]	700778	Sherpa 2.2.14	Run-3
$W(e\nu)$ + jets [CVeto,BVeto]	700779	Sherpa 2.2.14	Run-3
$W(\mu\nu)$ + jets [BFilter]	700780	Sherpa 2.2.14	Run-3
$W(\mu\nu)$ + jets [CFilter,BVeto]	700781	Sherpa 2.2.14	Run-3
$W(\mu\nu)$ + jets [CVeto,BVeto]	700782	Sherpa 2.2.14	Run-3
$Z(ee)$ + jets [BFilter]	700786	Sherpa 2.2.14	Run-3
$Z(ee)$ + jets [CFilter,BVeto]	700787	Sherpa 2.2.14	Run-3
$Z(ee)$ + jets [CVeto,BVeto]	700788	Sherpa 2.2.14	Run-3
$Z(\mu\mu)$ + jets [BFilter]	700789	Sherpa 2.2.14	Run-3
$Z(\mu\mu)$ + jets [CFilter,BVeto]	700790	Sherpa 2.2.14	Run-3
$Z(\mu\mu)$ + jets [CVeto,BVeto]	700791	Sherpa 2.2.14	Run-3

Table 5: List of all the MC simulation samples used in this thesis.

C p_{T} Dependencies of E_{iso} Distributions and Models

E_{iso} Distributions for Different p_{T} Intervals

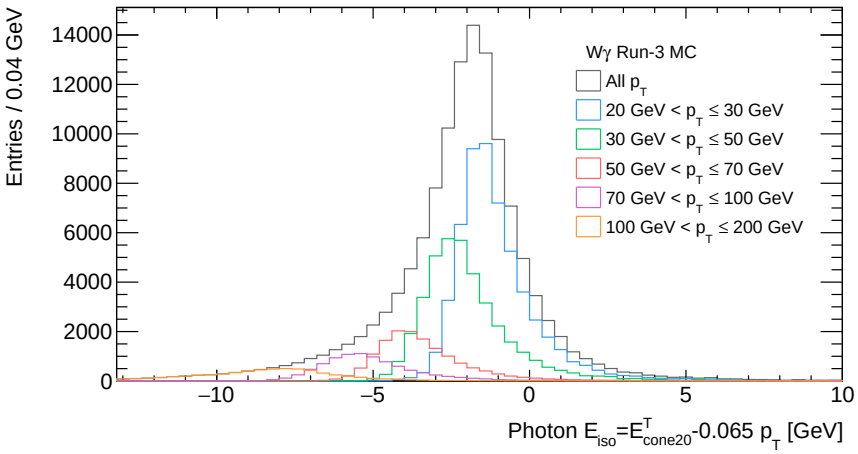

Figure 36: The E_{iso} distribution for the $W\gamma$ final state under Run-3 conditions for different p_{T} intervals. Just like for the $Z\gamma$ final state, the distributions shift to lower energies and get broader with increasing p_{T}, mostly due to the subtraction of $0.065 \cdot p_{\mathrm{T}}$ in the definition of $E_{\mathbf{iso}}$.

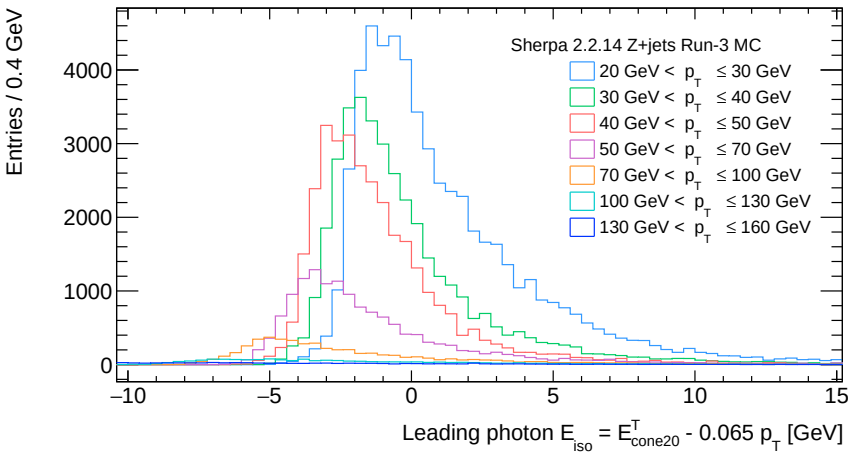

Figure 37: The E_{iso} distribution for the $Z\gamma$ final state under Run-3 conditions with a fake photon for different p_{T} intervals. Similar to the W+jets MC simulations, the distributions shift only slightly to lower energies and gets broader with higher p_{T} values.

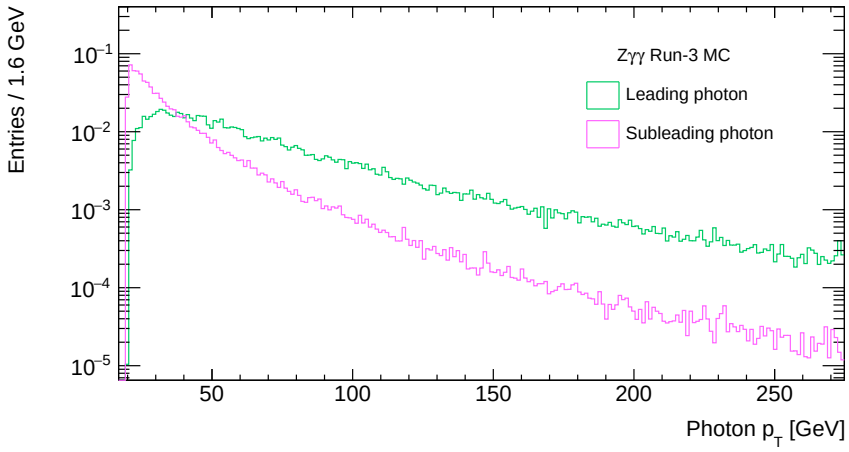

Figure 38: The p_{T} distribution of leading and subleading photons in the $Z\gamma\gamma$ final state. The leading and subleading photons in the $Z\gamma\gamma$ final state exhibit different p_{T} distributions.

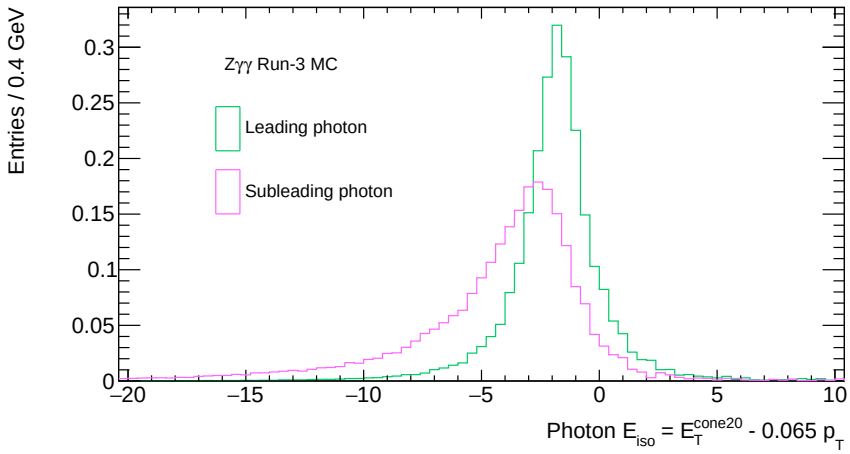

Figure 39: The E_{iso} distribution of leading and subleading photons in the $Z\gamma\gamma$ final state. Due to the strong p_{T} dependence, the E_{iso} distribution of leading and subleading photons have different shapes.

p_{T} Dependence of the One-dimensional Template for Real Photons

The p_{T} dependence of the one-dimensional extended DSCB templates for real photons is studied. The one-dimensional model is fitted to E_{iso} distributions of the $Z\gamma$ and $W\gamma$ final states for different p_{T} intervals. The obtained fit results for each of the parameters of the extended DSCB for the $W\gamma$ final state are shown in Figures 40 and 41. The p_{T} dependencies of each of the parameters can be approximated with linear or constant correlations. The approximated p_{T} dependencies are comparable to those derived from the $Z\gamma$ final state under Run-2 and used for the development of the generic template. This affirms that the generic template empirically derived from observation in final states under Run-2 conditions can also be applied to final states under Run-3 conditions. Yet, the linear and constant fits of the p_{T} dependence of the parameters show larger discrepancies than those observed in final states under Run-2 conditions. This is likely due to the fact that the model used for the E_{iso} distributions of final states under Run-2 conditions was an ordinary DSCB function. The model for E_{iso} distributions of real photons used in this thesis is an extended DSCB function with two additional power law tails. The model used in this thesis has therefore a larger set of parameter (four additional parameters) and consequently a higher instability of performed one-dimensional fits.

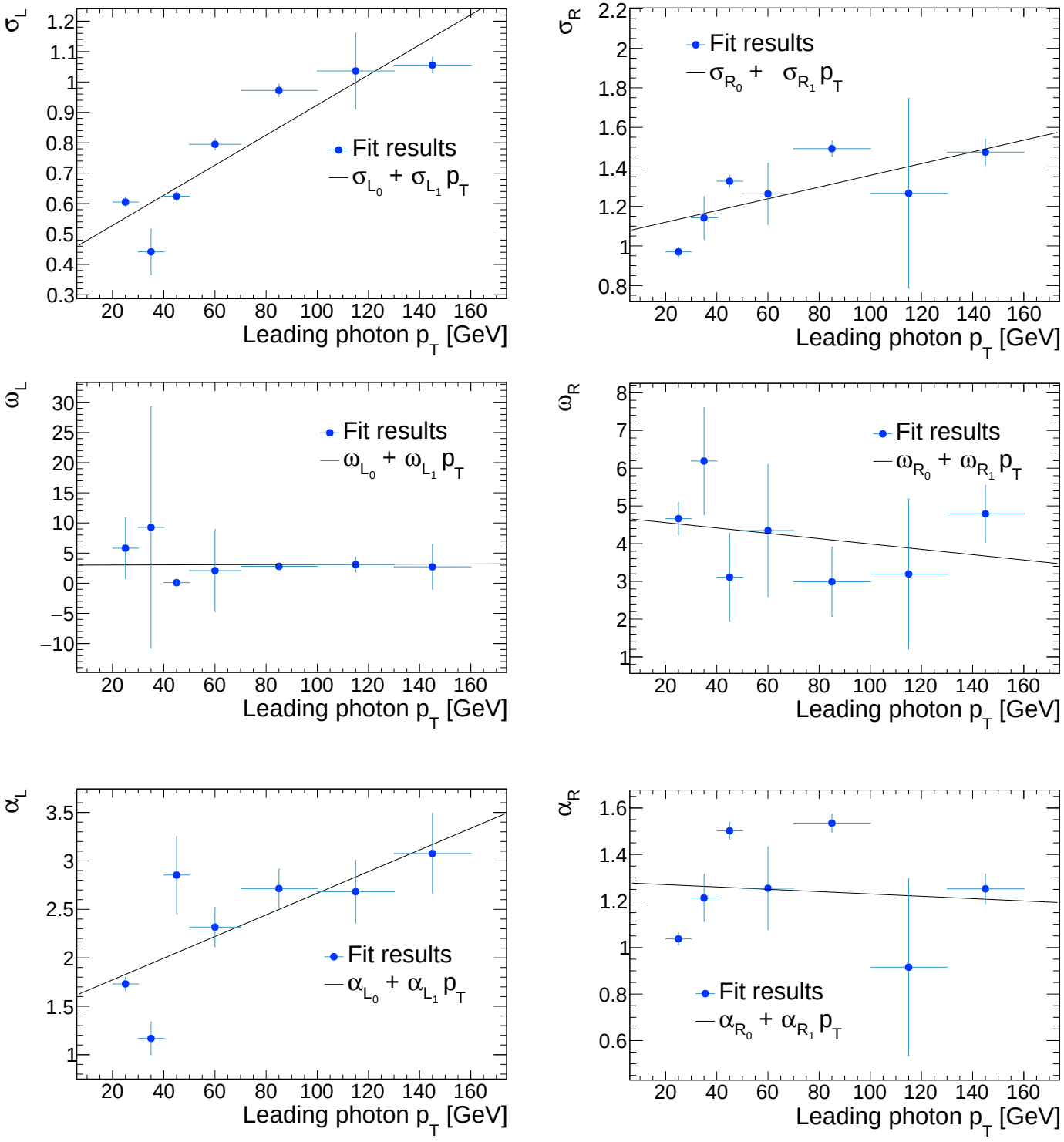

Figure 40: Study of the p_{T} dependence of the template for real photons for the $W\gamma$ final state. In the figures, the one-dimensional fit results model for the isolation of real photons for different p_{T} intervals are shown for six of the parameters of the model. The p_{T} dependence of each of the parameters can be approximated with either linear or constant correlations. However, large discrepancies are observed, especially for α_{L} and α_{R}. This is caused by the high instability of the one-dimensional fits which also explains the larger differences in the statistical uncertainties.

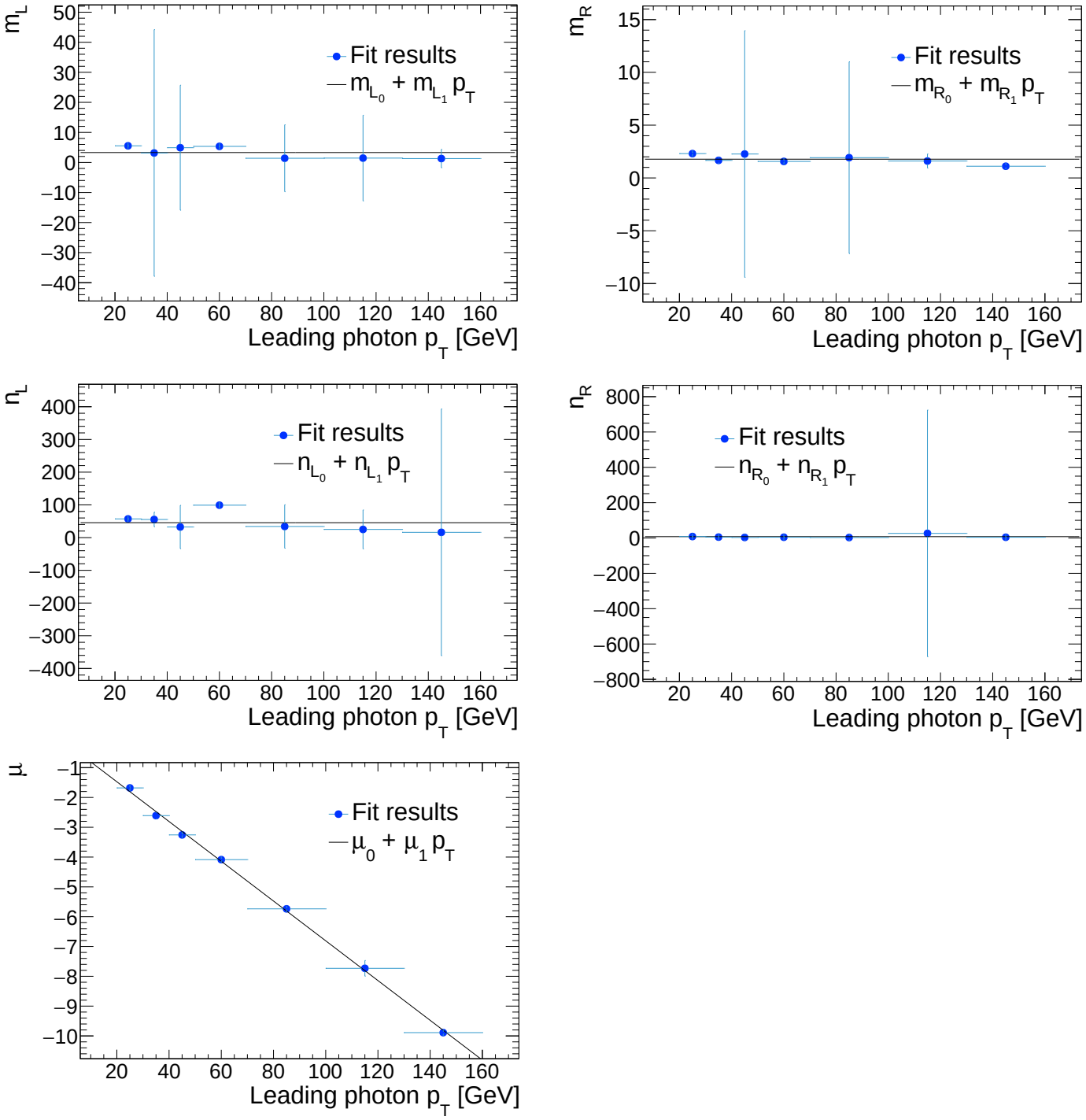

Figure 41: Study of the p_{T} dependence of the template for real photons for the $W\gamma$ final state. The p_{T} dependence of the exponents of the inner and outer tails of the extended DSCB function and its peak position μ are displayed. The tail exponents are approximately constant in p_{T} . The p_{T} dependence of μ can be approximated with a linear negative correlation.

D Optimal Parameters for the Generic Templates

The following tables summarise the optimal parameters for the generic templates extracted from different final states under Run-3 conditions. The variables denoted with 0 and 1 are defined by a linear dependence to p_{T}, e.g. $\alpha_0 + \alpha_1 p_{\mathrm{T}}$. The variables without this denotation are approximated to be constant in p_{T}, such as ρ_{L} and ρ_{R}. The constant variables are listed above the dashed line in the tables.

Table 6: Optimal parameters $\vec{\theta}_{opt}$ for the generic template extracted from $Z\gamma$ MC simulations.

Variable	**Value of optimal parameters**
m_L	$5.4608 \pm -$
m_R	$0.016657 \pm -$
n_L	$31.683 \pm -$
n_R	$4.4955 \pm -$
α_{L_0}	1.2511 ± 0.844
α_{L_1}	0.0048755 ± 0.778
α_{R_0}	1.0616 ± 0.0684
α_{R_1}	0.00068862 ± 0.00275
β_{L_0}	9.3535 ± 27300
β_{L_1}	-0.000012701 ± 4.03
β_{R_0}	17.543 ± 904
β_{R_1}	-0.0048395 ± 0.00209
σ_{L_0}	0.43399 ± 1.11
σ_{L_1}	0.0021259 ± 0.018
σ_{R_0}	0.77896 ± 0.124
σ_{R_1}	0.0047721 ± 0.00849
μ_{L_0}	0.0012649 ± 0.569
μ_{R_1}	-0.071325 ± 0.00138

D Optimal Parameters for the Generic Templates

Table 7: Optimal parameters $\vec{\theta}_{opt}$ for the generic template extracted from $W\gamma$ MC simulations.

Variable	**Value of optimal parameters**
m_L	$0.76720 \pm -$
m_R	$0.16644 \pm -$
n_L	$59.851 \pm -$
n_R	$6.1073 \pm -$
α_{L_0}	1.5024 ± 0.254
α_{L_1}	0.0044432 ± 0.00371
α_{R_0}	0.84055 ± 0.256
α_{R_1}	0.0010363 ± 0.00192
β_{L_0}	1.2744 ± 1.45
β_{L_1}	0.26761 ± 0.0693
β_{R_0}	9.9969 ± 0.629
β_{R_1}	0.13720 ± 0.0538
σ_{L_0}	0.49811 ± 0.0762
σ_{L_1}	0.0016648 ± 0.000816
σ_{R_0}	0.74024 ± 0.247
σ_{R_1}	0.0054803 ± 0.00197
μ_{L_0}	0.012114 ± 0.121
μ_{R_1}	-0.071541 ± 0.00117

Table 8: Optimal parameters $\vec{\theta}_{opt}$ for the generic template extracted from Z+jets MC simulations.

variable $\vec{\theta}$	**value of optimal parameters**
ρ_L	$-0.31366 \pm -$
ρ_R	$0.010638 \pm -$
α_0	0.584278 ± 0.00201901
α_1	$-0.00198678 \pm 4.77205 \times 10^{-5}$
μ_0	-0.254064 ± 0.00321588
μ_1	$-0.0387478 \pm 8.84392 \times 10^{-6}$
σ_0	1.13337 ± 0.00222695
σ_1	$0.024913 \pm 4.82479 \times 10^{-5}$

Table 9: Optimal parameters $\vec{\theta}_{opt}$ for the generic template extracted from W+jets MC simulations.

variable $\vec{\theta}$	**value of optimal parameters**
ρ_{L}	$-0.22585 \pm -$
ρ_{R}	$0.011587 \pm -$
α_0	0.551968 ± 1.19365
α_1	$-0.00143957 \pm 0.0875327$
μ_0	-0.449085 ± 6.3094
μ_1	-0.0345168 ± 0.411175
σ_0	1.04796 ± 0.104414
σ_1	0.0275221 ± 0.125786

E Template Comparisons for Real and Fake Photon Candidates

The extracted templates for real and fake photons are compared to other final states. For this no fit is needed, only the extracted generic template is multiplied by the corresponding p_{T} distribution of the photon in the final state to which the template is compared. The following figures depict the projection of the two-dimensional template onto the p_{T} and E_{iso} axes of the photons in the compared final state.

Template Comparisons of Real Photon Candidates

In this section of the Appendix the rest of the comparisons of templates for real photons are displayed.

$Z\gamma$ and $W\gamma$ Templates Comparisons to the $Z\gamma\gamma$ Final State

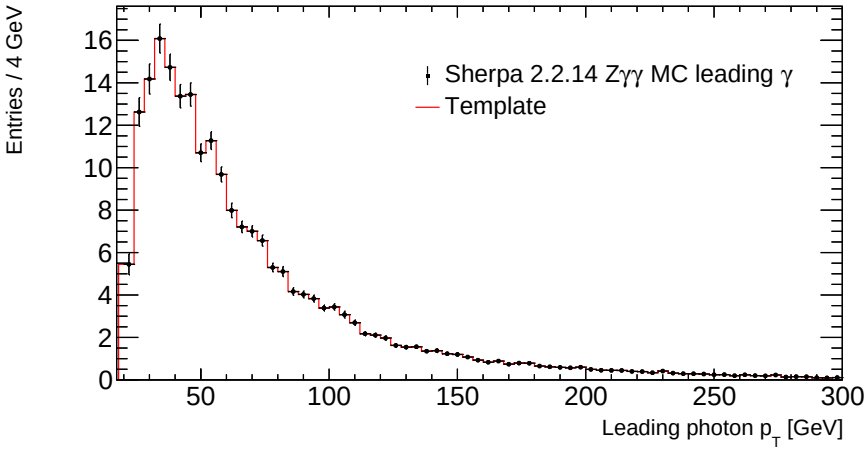

Figure 42: The template projected onto the p_{T} axis of the leading photon in the $Z\gamma\gamma$ final state. The p_{T} distribution is modelled with a binned histogram.

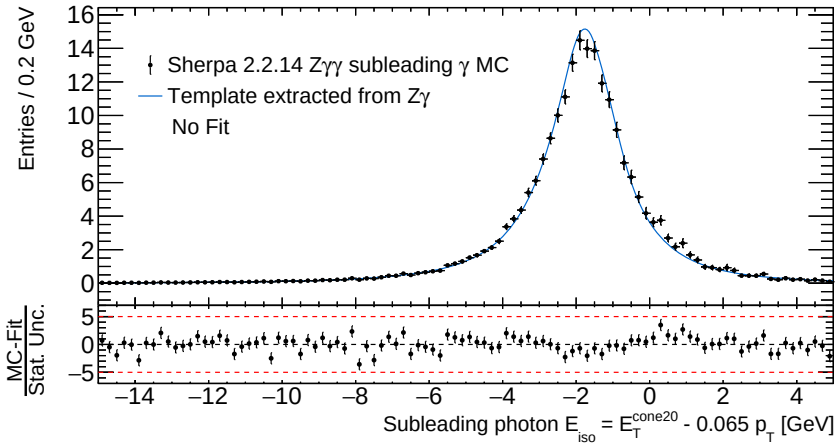

Figure 43: The template derived from the $Z\gamma$ final state compared to the distribution of the subleading photon in the $Z\gamma\gamma$ final state.

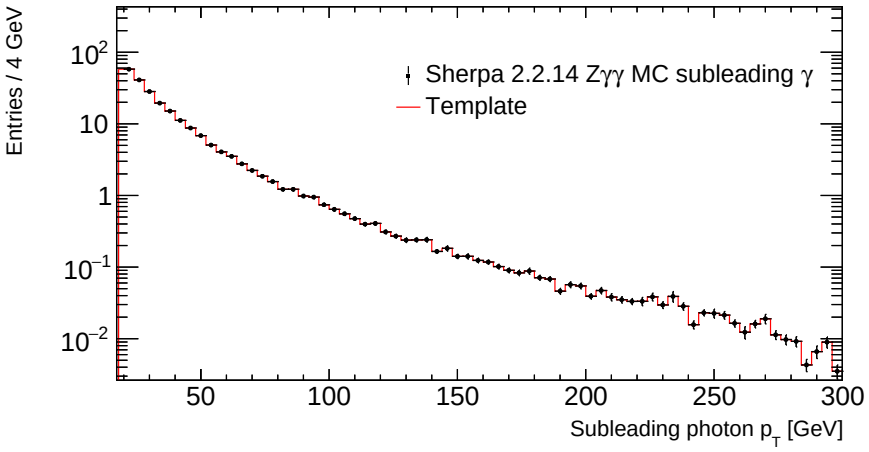

Figure 44: The template projected onto the p_{T} axis of the subleading photon in the $Z\gamma\gamma$ final state.

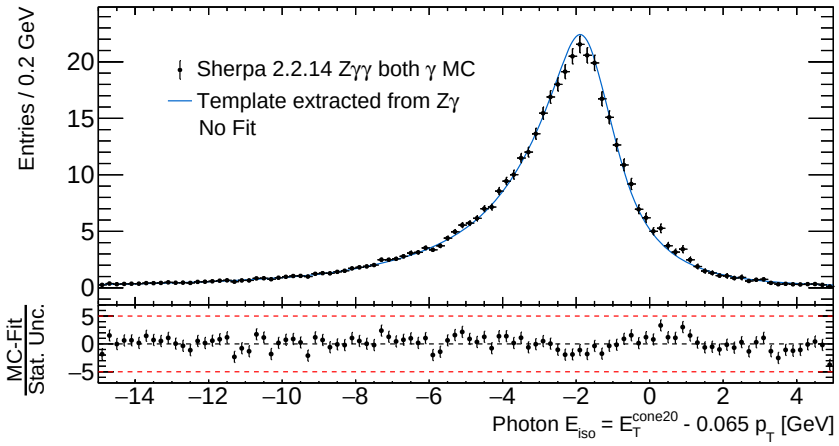

Figure 45: The template derived from the $Z\gamma$ final state compared to the E_{iso} distribution of a combination of the leading and subleading photons in the $Z\gamma\gamma$ final state.

E Template Comparisons for Real and Fake Photon Candidates

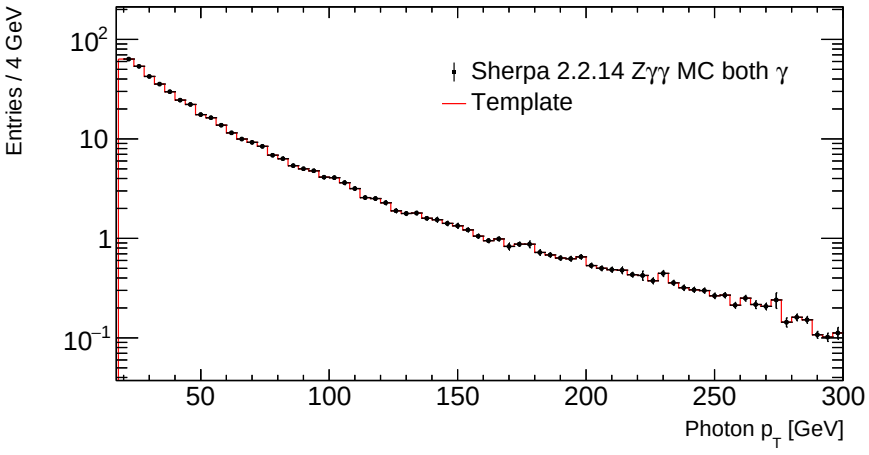

Figure 46: The template projected onto the p_{T} axis of the combination of photons in the $Z\gamma\gamma$ final state.

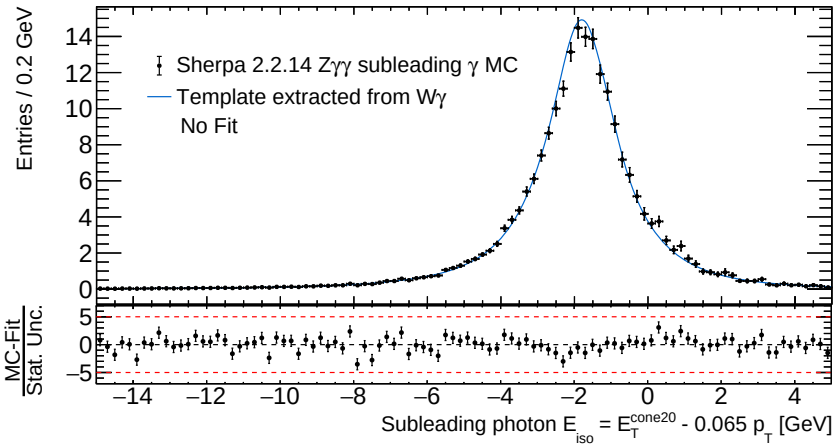

Figure 47: The Template derived from the $W\gamma$ final state compared to the E_{iso} distribution of the subleading photon in the $W\gamma\gamma$ final state.

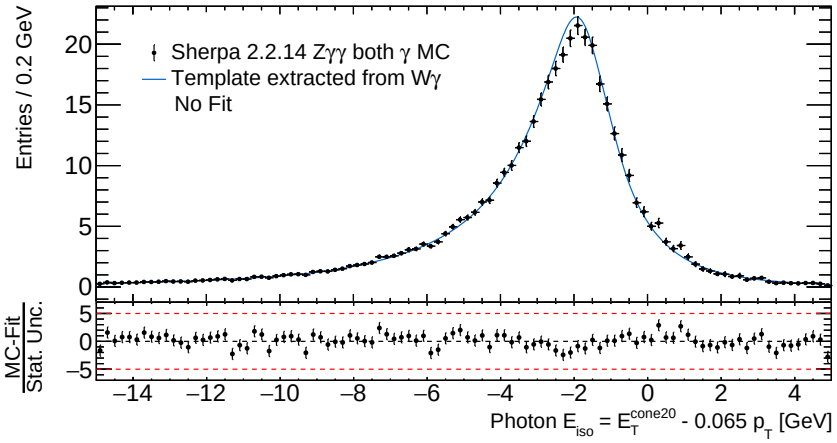

Figure 48: The template with optimal parameters extracted from the $W\gamma$ final state is applied to the $Z\gamma\gamma$ final state photons E_{iso} distributions.

$Z\gamma$ and $W\gamma$ Templates Comparisons to the $W\gamma\gamma$ Final State

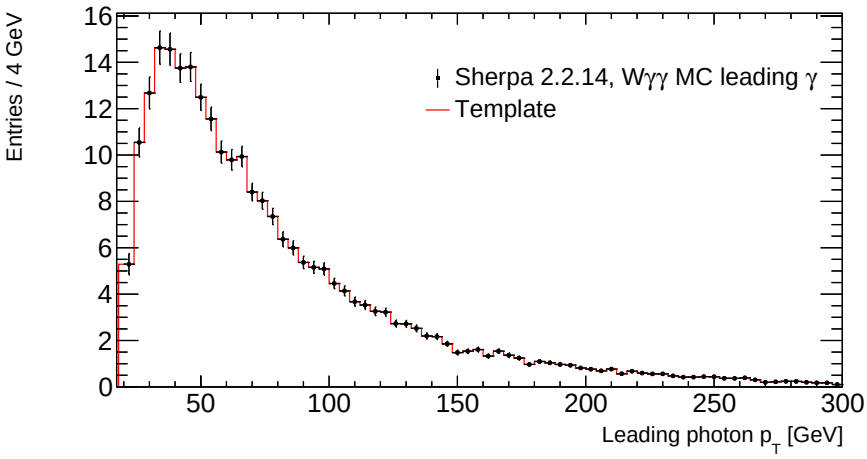

Figure 49: The template projected onto the p_{T} axis of the leading photon in the $W\gamma\gamma$ final state.

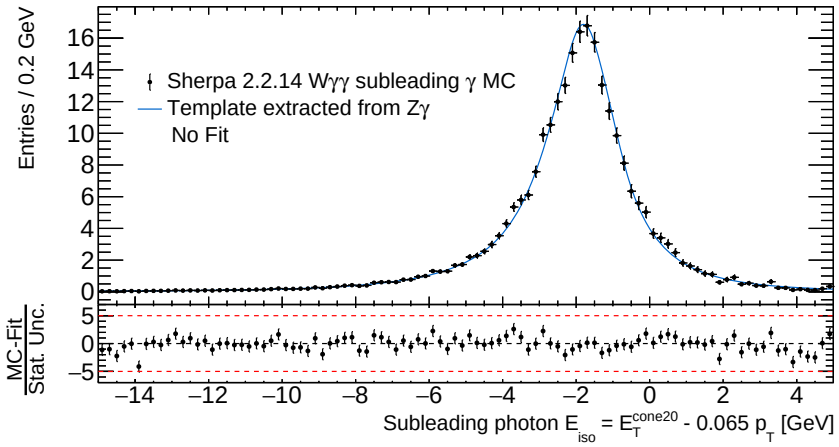

Figure 50: The Template derived from the $Z\gamma$ final state compared to the E_{iso} distribution of the subleading photon in the $W\gamma\gamma$ final state.

E Template Comparisons for Real and Fake Photon Candidates

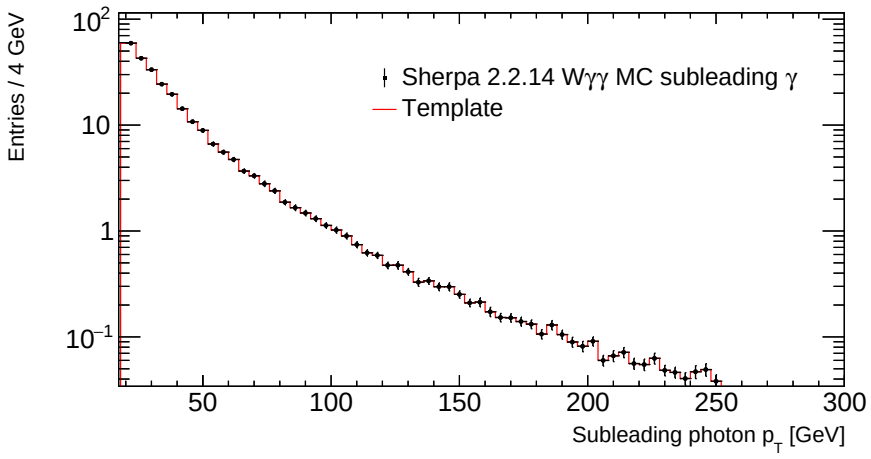

Figure 51: The template projected onto the p_{T} axis of the subleading photon in the $W\gamma\gamma$ final state.

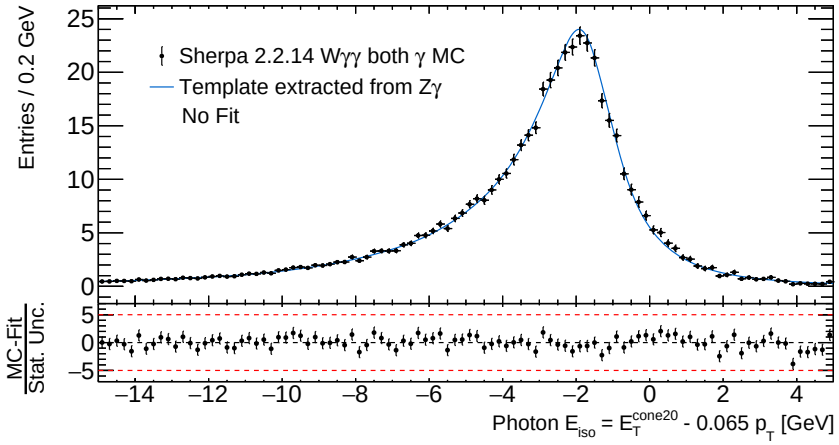

Figure 52: The template extracted from the $Z\gamma$ final state applied to the $Z\gamma\gamma$ final state photons E_{iso} distributions.

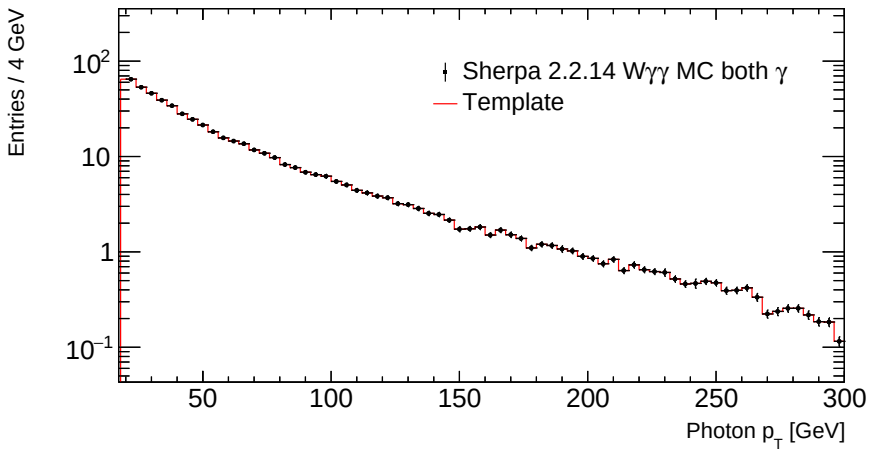

Figure 53: The template projected onto the p_{T} axis of the subleading photon in the $W\gamma\gamma$ final state.

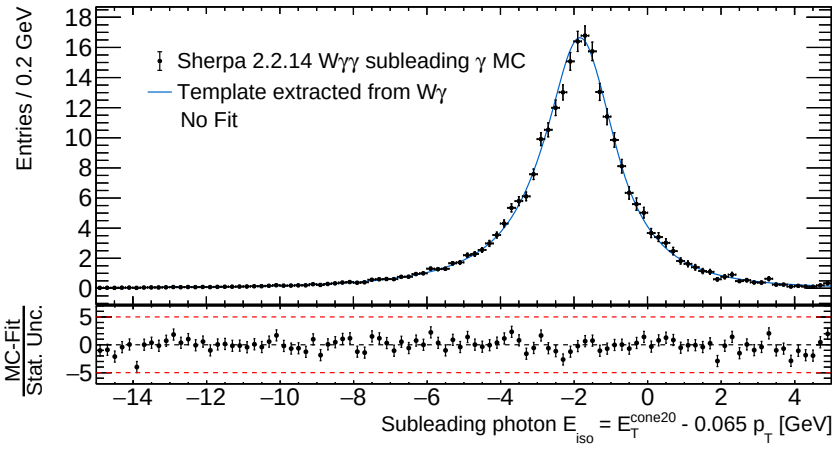

Figure 54: The Template derived from the $W\gamma$ final state compared to the E_{iso} distribution of the subleading photon in the $W\gamma\gamma$ final state.

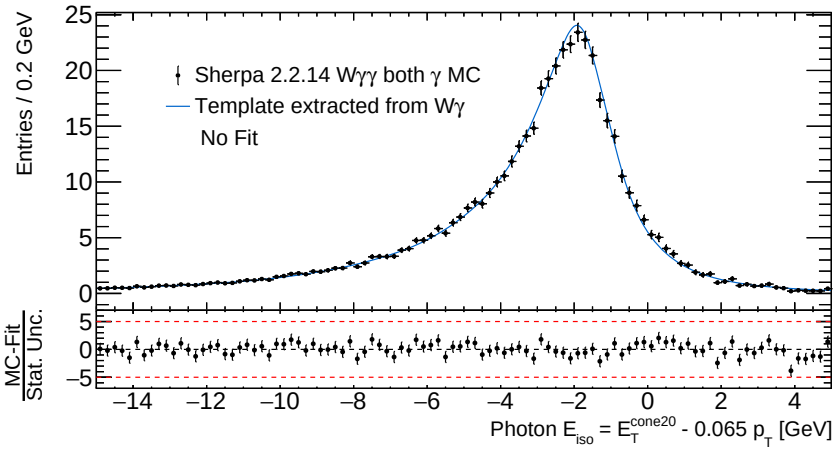

Figure 55: The template extracted from the $W\gamma$ final state is applied to the $W\gamma\gamma$ final state photons E_{iso} distributions.

Template Comparisons of Fake Photon Candidates

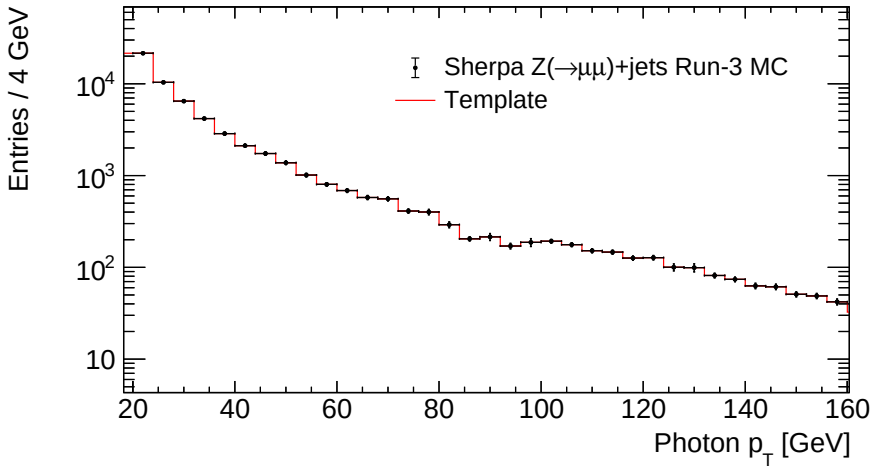

Figure 56: Projection of the fit results for the extraction of the template for fake photons onto the p_{T} axis. Analogue to the real photons, the p_{T} distribution of fake photons is modelled with a binned histogram.

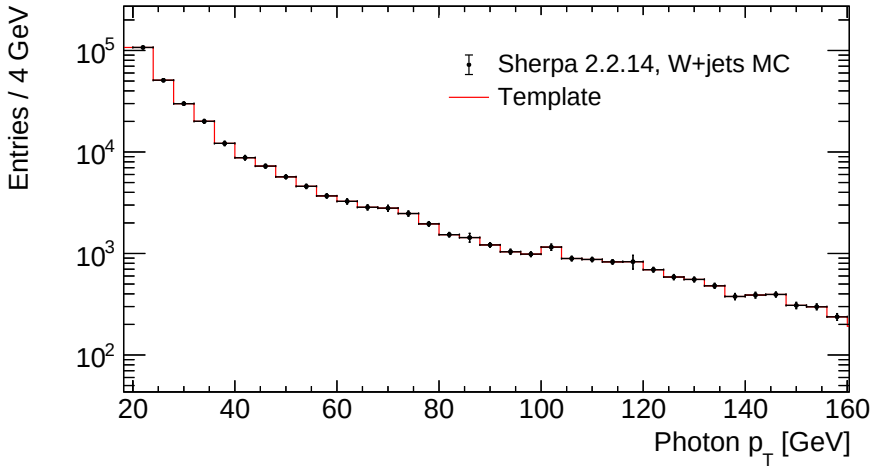

Figure 57: Projection of the fit results for the extraction of the template for fake photons onto the p_{T} axis. Analogue to the real photons, the p_{T} distribution of the fake photons is modelled with a binned histogram.

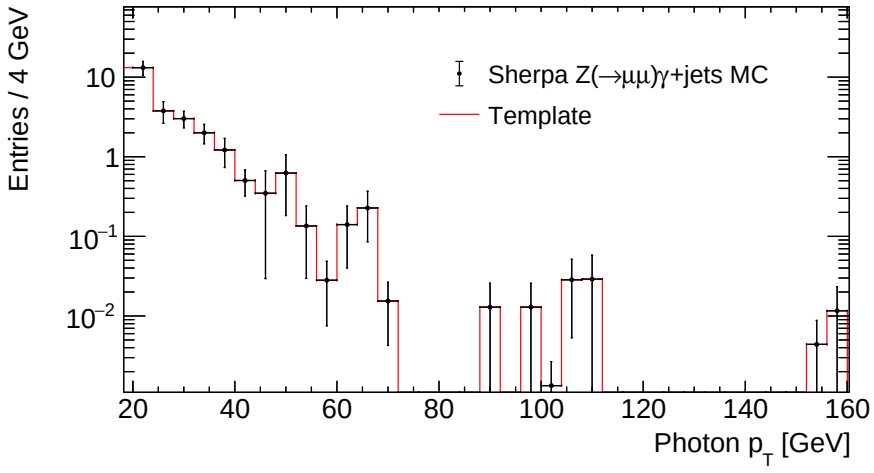

Figure 58: Projection of the template for fake photons onto the p_{T} axis of a combination of the fake photons in final state Zjy and Zyj. Analogue to the real photons, the p_{T} distribution of fake photons is modelled with a binned histogram.

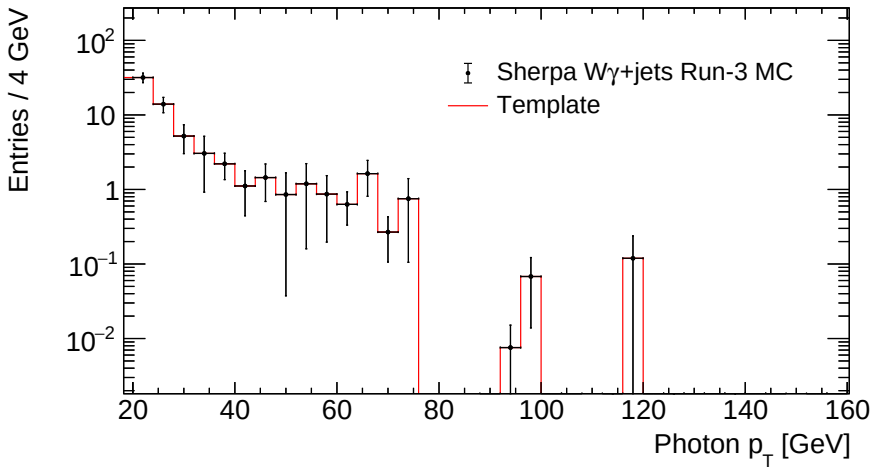

Figure 59: Projection of the template for fake photons onto the p_{T} axis of a combination of the fake photons in final state Wjy and Wyj. Analogue to the real photons, the p_{T} distribution of fake photons is modelled with a binned histogram.

List of Abbreviations

SM	Standard Model
LHC	Large Hadron Collider
MC	Monte Carlo
LAr	Liquid Argon
ID	Identification
ISO	Isolation
WP	Working Point
ISR	Initial state radiation
FSR	Final state radiation
DSCB	Double-sided Crystal Ball
EM	Electromagnetic
topo-cluster	Topological cluster

References

[1] Mark Thomson. *Modern particle physics*. Cambridge University Press, 2013. ISBN: 978-1107034266. URL: https://www.cambridge.org/highereducation/books/modern-particle-physics/CDFEBC9AE513DA60AA12DE015181A948#overview.

[2] Michael Hauschild. *Exploring the Large Hadron Collider - CERN and the Accelerators*. Springer, 2022. ISBN: 978-3658332921. URL: https://link.springer.com/book/10.1007/978-3-658-33293-8.

[3] Tobias Heintz. "Improvement of the template fit method for the fake photon background estimation at ATLAS". Bachelorarbeit. Universität Heidelberg, Aug. 2023.

[4] Lyndon Evans and Philip Bryant. "LHC Machine". In: *Journal of Instrumentation* 3.08 (Aug. 2008), S08001. DOI: 10.1088/1748-0221/3/08/S08001. URL: https://dx.doi.org/10.1088/1748-0221/3/08/S08001.

[5] G. Aad et al. "The ATLAS Experiment at the CERN Large Hadron Collider". In: *JINST* 19 (2024). URL: https://iopscience.iop.org/article/10.1088/1748-0221/19/05/P05063.

[6] "The ATLAS Collaboration". "Luminosity determination in pp collisions at $\sqrt{s} = 13$ TeV using the ATLAS detector at the LHC". In: *The European Physical Journal C* 83.10 (2023). ISSN: 1434-6052. DOI: 10.1140/epjc/s10052-023-11747-w. URL: http://dx.doi.org/10.1140/epjc/s10052-023-11747-w.

[7] The ATLAS Collaboration et al. "The ATLAS Experiment at the CERN Large Hadron Collider". In: *JINST* 3 (2008). URL: https://iopscience.iop.org/article/10.1088/1748-0221/3/08/S08003.

[8] Riccardo Maria "Bianchi and ATLAS Collaboration". "Images from the paper: "The ATLAS Experiment at the CERN Large Hadron Collider: A Description of the Detector Configuration for Run 3". In: "" (2024). "General Photo". URL: https://cds.cern.ch/record/2900788.

[9] The ATLAS Collaboration. "The ATLAS Inner Detector commissioning and calibration". In: *Eur. Phys. J. C* (2010). URL: https://cds.cern.ch/record/1262789/files/EurPhysJC.3FBE7E53d01.

[10] ATLAS Collaboration. *Operation and performance of the ATLAS tile calorimeter in LHC Run 2*. 2024. arXiv: 2401.16034 [hep-ex]. URL: https://arxiv.org/abs/2401.16034.

[11] G. Aad et al. "Electron and photon performance measurements with the ATLAS detector using the 2015–2017 LHC proton-proton collision data". In: *JINST* 14 (2019). URL: https://iopscience.iop.org/article/10.1088/1748-0221/14/12/P12006.

[12] N. Buatthaisong. "Electron/Photon Ambiguity Resolution Using Neural networks for ATLAS Experiment". In: (2019). URL: https://www.desy.de/f/students/2019/reports/nutthawara.buatthaisong.pdf.gz.

[13] Gregor Geßner on behalf of the ATLAS collaboration. "Photon identification with the ATLAS detector". In: *PoS* (2017). URL: https://cds.cern.ch/record/2281395/files/ATL-PHYS-PROC-2017-105.

[14] Morad Aaboud et al. "Measurement of the photon identification efficiencies with the ATLAS detector using LHC Run 2 data collected in 2015 and 2016". In: *Eur. Phys. J. C* 79.3 (2019), p. 205. DOI: 10.1140/epjc/s10052-019-6650-6. arXiv: 1810.05087 [hep-ex].

[15] Morad Aaboud et al. "Electron reconstruction and identification in the ATLAS experiment using the 2015 and 2016 LHC proton-proton collision data at $\sqrt{s} = 13$ TeV". In: *Eur. Phys. J. C* 79.8 (2019), p. 639. DOI: 10.1140/epjc/s10052-019-7140-6. arXiv: 1902.04655 [physics.ins-det].

[16] Philipp Ott. "Measurement of $Z\gamma\gamma$ production in pp collisions at $\sqrt{s} = 13$ TeV with the ATLAS detector". PhD thesis. Universität Heidelberg, 2023.

[17] Georges Aad et al. "The ATLAS trigger system for LHC Run 3 and trigger performance in 2022". In: *JINST* 19.06 (2024), P06029. DOI: 10.1088/1748-0221/19/06/P06029. arXiv: 2401.06630 [hep-ex]. URL: https://iopscience.iop.org/article/10.1088/1748-0221/19/05/P05063/pdf.

[18] The ATLAS Collaboration. "Software Performance of the ATLAS Track Reconstruction for LHC Run 3". In: *Computing and Software for Big Science* 8.1 (Apr. 2024). ISSN: 2510-2044. DOI: 10.1007/s41781-023-00111-y. URL: http://dx.doi.org/10.1007/s41781-023-00111-y.

[19] Gabriella Pásztor. *The Upgrade of the ATLAS Electron and Photon Triggers towards LHC Run 2 and their Performance*. 2015. arXiv: 1511.00334 [hep-ex]. URL: https://arxiv.org/abs/1511.00334.

[20] Tomasz Skwarnicki. “A study of the radiative CASCADE transitions between the Upsilon-Prime and Upsilon resonances”. PhD thesis. Cracow, INP, 1986.

[21] Private communication Tobias Heintz. 2024.

[22] A. D. Bukin. *Fitting function for asymmetric peaks*. 2007. arXiv: 0711.4449 [physics.data-an]. URL: https://arxiv.org/abs/0711.4449.

[23] J. Saxon. “”Discovery of the Higgs Boson, Measurements of its Production, and a Search for Higgs Boson Pair Production””. In: (2014). URL: https://cds.cern.ch/record/1746004.

Acknowledgements

Firstly, I would like to thank Prof. Dr. Hans-Christian Schultz-Coulon for his supervision. Additional thanks go to Prof. Dr. Belina von Krosigk for kindly agreeing to be my second examiner. I would also like to express my gratitude to Rainer Stamen for his supervision and insightful ideas. Thanks go to all the members of the ATLAS research group at KIP for the supportive environment and inspiring discussions. Special thanks to my supervisor, Tobias Heintz for his helpful support and guidance.

Erklärung

Ich versichere, dass ich diese Arbeit selbstständig verfasst und keine anderen als die angegebenen Quellen und Hilfsmittel benutzt habe.

Heidelberg, den 02.09.2024,